UNIVERSITÀ DEGLI STUDI DI PALERMO

PhD program in "*Technology and Science for Human Health*"

Department of Health Promotion, Mother and Child Care, Internal Medicine and Medical Specialties

University of Palermo

Mandrel-less fabrication of biomimetic electrospun microfiber wires for tissue engineering applications

PhD CANDIDATE

Arianna Adamo, MS

PhD PROGRAM COORDINATOR

Prof. Maurizio Leone

MENTOR

Prof. Antonio D'Amore

TUTORS

Prof. Giulio Ghersi

Prof. Gaetano Burriesci

XXXIII

2019/2020

In hopes that this work may, in some way, contribute to the research progress.

Index

LIST OF FIGURES

NOMENCLATURE

AHVs – Atrio-ventricular Heart Valves

ANOVA – Analysis of Variance

AVMA –American Veterinary Association

BECT – Bioengineered Chordae Tendineae

BMM – Bone Marrow-derived Macrophages

BSA – Bovine Serum Albumin

CT – Chordae Tendineae

DAPI – 4′,6-diamidino-2-phenylindole

DMEM – Dulbecco's modified eagle medium

ECM – Extracellular Matrix

ePTFE – Expanded Polytetrafluoroethylene

ES – Electrospun

FBS – Fetal Bovine Serum

GAGs – Glycosaminoglycans

H&E – Hematoxylin and Eosin

HEPES – 4-(2-hydroxyethyl)-1-piperazineethanesulfonic acid

HFIP – Hexafluoro Isopropanol

HSD – Honestly Significant Difference

IF – Immunofluorescence

IHC – Immunohistochemistry

IL – Interleukin

INFγ – Interferon gamma

iNOS – Inducible Nitric Oxide Synthase

LPS – Lipopolysaccharide

M1 macrophages – Pro-inflammatory macrophages phenotype

M2 macrophages – Anti- inflammatory macrophages phenotype

MV – Mitral Valve

PBS – Phosphate-Buffered Saline

PCUU – Poly(carbonate urethane) urea

PDS II – Polydioxanone

PEUU – Poly(ester urethane) urea

PEUU Cast – PEUU casted

PEUU Cast wires – PEUU casted wires

PEUU ES – PEUU electrospun

PEUU ES wires – PEUU electrospun wires

PFA – Paraformaldehyde

PGA – Polyglycolic Acid

PPL – Polypropylene

SEM – Scanning Electron Microscopy

TBST – Tris-buffered saline with 0.1% Tween® 20 Detergent

Th – Lymphocyte T-helper

TNF – Tumor Necrosis Factor

ABSTRACT

This study introduces a novel mandrel-less electrodeposition method and a novel electrode prototypes useful for tissue engineering applications. More specifically, in this study a novel fabrication protocol to electrospun fibers-based chords, with length spanning from 2 cm to virtually no limitations on longitudinal length, is presented.

For the first part of this study, Poly(ester urethane) urea (PEUU) was used to fabricate, by electrodeposition technique, continuous microfiber wires with controlled micro-architecture and tunable mechanics. A novel apparatus to process degradable or non-degradable polymers was used. Soft tissue injuries are common in daily clinical and surgical practice. Outcomes of degradable and non-degradable suture materials are often affected by mechanical mismatch, excessive fibrosis and inflammation. Microfiber wire morphology and mechanical properties have been characterized by scanning electron microscopy and uniaxial tensile test respectively. Furthermore, the *in vitro* response of mouse bone marrow-derived macrophages (BMM) to PEUU degradation products, PEUU electrospun (ES) and casted (Cast) 2D scaffold configuration and PEUU ES wires was evaluated by immunoblotting and immunolabeling. Moreover, the host response to electrospun wires *in vivo* was tested: fifteen rats, randomized in 5 groups, received a 2 cm infra-scapular incision and the skin was closed using PEUU microfiber and cast wires and the most common suture materials used (polyglycolic acid, polydioxanone and polypropylene). After one month, mechanical and histological evaluation of explants and suture wires was performed. *In vitro* results have shown an anti-inflammatory macrophage response associated to PEUU ES 2D scaffolds and 3D wires. *In vivo*, PEUU ES wires group showed better mechanical performance compared to the other groups, a favorable collagen remodeling comparable to the healthy group and a mild host response reaction. These results suggest that microfiber wires reduce macrophage pro-inflammatory response and improve collagen deposition, which make it an ideal candidate for soft tissue suture applications.

The second part of this study is focused on creating a biomimetic engineered chordae tendineae (BECT) using Poly(carbonate urethane) urea (PCUU). The mandrel-less electrodeposition methodology is used to mimic the macro and micro architecture of native chordae tendineae (CT). The voltage generated by

the two facing electrodes will induce a deposition of highly aligned microscopic fibers that duplicate native tissue anatomy and function structure. Current methods for CT replacement do not recapitulate the microarchitecture nor the mechanics of the native CT and do not promote healthy tissue regeneration. Human and porcine CT were harvested and tested to evaluate mechanical and histological native tissue structure. PCUU was used to fabricate BECT via mandrel-less electrodeposition. Moreover, BECT were micro-integrated with NIH-3T3 rat fibroblasts. Micro-integrated BECT were divided in 3 groups: static culture in plate, tension culture in plate and dynamic culture using a stretch bioreactor. All groups were conditioned for 1 week. Finally, scanning electron microscopy (SEM), uniaxial tensile testing and histological evaluation were performed to compare native tissue and BECT micro-architecture and mechanical properties. BECT mimicked native CT shape, diameter, and length. SEM analysis showed highly aligned fiber microstructure recapitulating the arrangement observed in native CT. BECT mechanical characterization showed a lower elastic modulus than native tissue that increased with dynamic conditioning for cell micro-integrated BECT. The histology of cell-seeded BECT demonstrated cell adhesion and infiltration after one week. This mandrel-less electrodeposition method allows the bio-fabrication of BECT that demonstrate the ability to recapitulate native CT structure with use of a scaffold. Micro-integration preliminary data provided evidence of cell proliferation and viability, demonstrating an early proof-of concept for potential host cell recruitment.

INTRODUCTION

Electrospinning for tissue engineering applications

Electrospinning is a broadly used technique which involves an electrohydrodynamic process during which a liquid droplet is electrified to generate a jet, followed by stretching and elongation to generate fibers[6]. The basic set up for electrospinning is simple and could be accessible to almost every laboratory. Major components are the high-voltages generators, a syringe-pump, a spinneret and a conductive collector (**Figure 1**A). During electrospinning the polymer drop extruded from the spinneret, electrically charged, turn into a Taylor cone, from which a charged jet is ejected. The polymeric jet initially extends straight and then, because the bending instabilities, undergoes whipping motions[66] (**Figure 1**B).

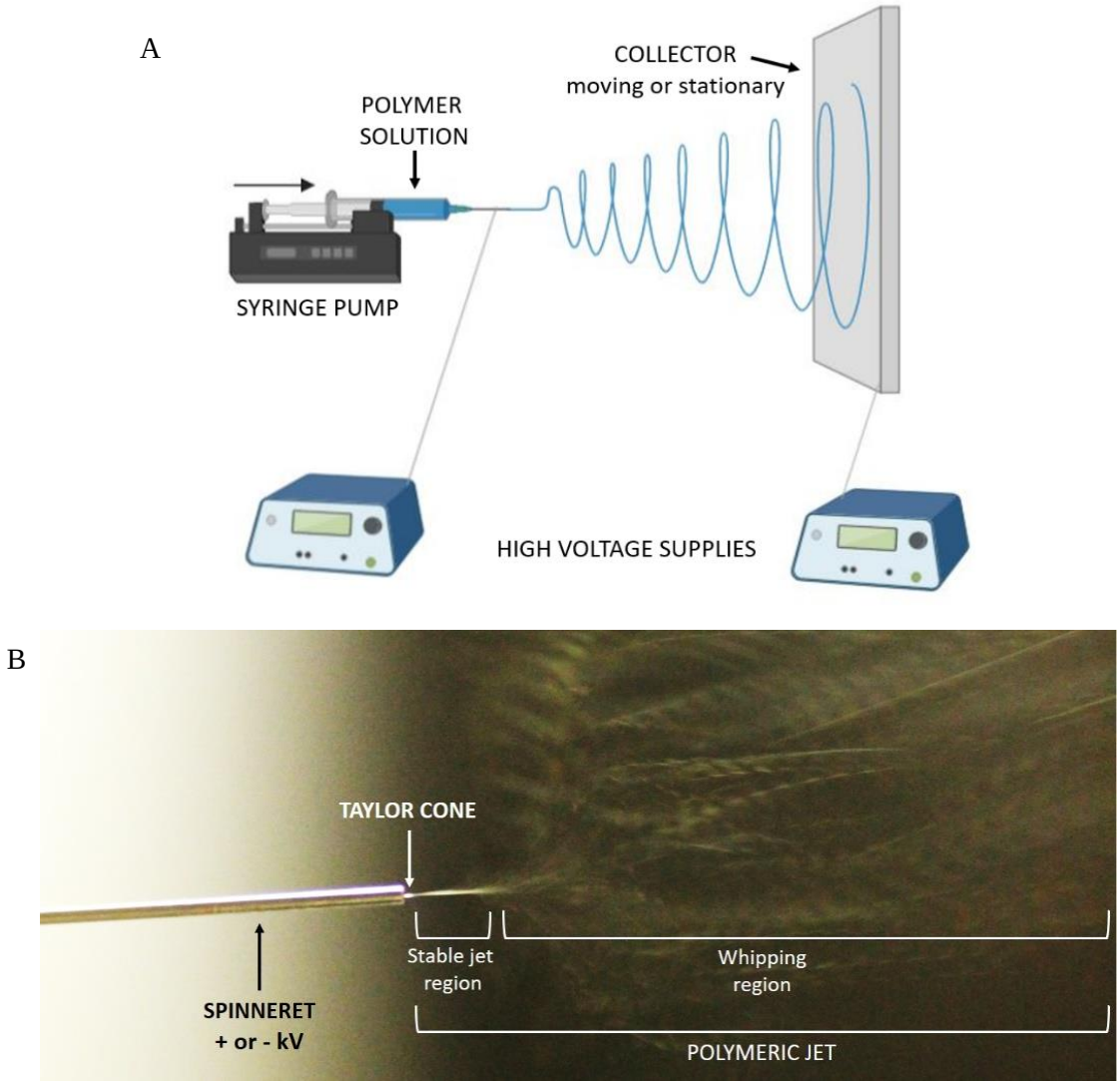

Figure 1 Electrospinning process*. A) Basic electrospinning set up B) High-speed photographs showing the evolution of PEUU polymeric jet.*

The electrospinning process can be manipulated by a number of variables. Doshi and Reneker classified the parameters that control the process in terms of solution properties, controlled variables, and ambient parameters[26]. In fact, the morphology of the fibers onto the target is heavily dependent on the qualities of the polymer solution, such as solution concentration, polymer molecular weight and viscosity, as well as processing controllable variables, like polymer flow rate, collector composition and geometry, distance between spinneret and collector, and even ambient conditions, for instance humidity and temperature[51]. These parameters, which affect polymer chain interactions within solution, are responsible for the ability of a solution to be electrospun into intact fibers.

Over the past two decades, due to its ability to produce continuous fibers in the submicron range, electrospinning has seen a tremendous increase in research and commercial attention, especially in tissue engineering applications. Such size scales are of particular interest in the medical field, as they encompass the same order of magnitude of diameters found in native extracellular matrix (ECM) three-dimensional environment, which was supposed to be attractive for supporting viable cells. Electrospun scaffolds have been investigated for the repair of biological tissue. Since these constructs have a high surface area to volume ratio, they provide more space for cell invasion, proliferation and differentiation, in order to regenerate the physiological functions of native tissue[41]. The ultrafine fibrous scaffolds, produced by electrodeposition techniques, have been demonstrated to be suitable substrate for types of cells *in vitro* and to improve the host cell recruitment *in vivo*[41]. Electrospun fibers mats function as temporary support during the ex-novo tissue growing and ECM regeneration.

Controlling electrospun topology

Electrospinning, in its basic form, is known to be a chaotic process. In the field of bioengineering, aligned fibers are of great importance as a number of tissues possess pronounced structural and mechanical anisotropy, including tendons[56], hearth valves[12, 18] and nerves[50]. Further, cells were able to grow in the direction of fiber orientation, forming a three-dimensional and multicellular network according to the architecture of the nanofibrous structure[13, 41, 55, 70]. Several research works have enabled greater control using modifications of the collector, electrodes with patterns or moving target[62]. Courtney et al. have demonstrated that by rotating the drum target with a tangential velocity faster than

the speed that the fibers accumulate, they can be physically pulled into alignment with the rotation[15]. However, despite the efforts made to move away from just collecting random fiber mesh there is still no proper control of the resultant product. In order to achieve consistent patterns using electrospinning it is essential to control the fiber deposition point. Several electrospinning set-ups have been proposed to control the deposition area[64]. However, the inability to accurately deposit fibers is still a major drawback in the advances of electrospinning. Applications such as fabricating electrospun filaments and yarn are highly interesting because they can be used for a variety of biocompatible scaffolds, for medical suture or for tendon replacement. Despite the enormous potential of fibrous scaffold little efforts have been made to fabricate a continuous electrospun filament that can mimic the hierarchical ECM architecture and the mechanical properties of the tissue[7]. So far, continuous electrospun filaments have been created through the use of different collectors and different fabrication techniques. Khil, Smit, Teo and Yousefzadeh have used liquid surfaces: electrospun fibers coagulated in a bath in order to eliminate electrical charges and the fiber bundles formed on the liquid surface were drawn out under the action of liquid surface tension[38, 58, 63, 69]. Dabirian developed an electrospinning set-up in which fibers were collected using the effect of gravitational and repulsive forces: on one side the fibers were placed into the yarn body in a rotating take up unit, on the other side, because of a few remained charges, fibers were pulled to a negative charged flat collector[23]. Bazbouz applied a mechanism with two perpendicularly electrically grounded collector disks and the yarn was wound on another take-up disk[5]. Ali, Afifi, He and more recently Liao, used a static funnel with multiple charged nozzles or rotating funnels and a single nozzle[2, 4, 44, 49], obtaining highly twisted microfiber yarns. Yan and Hajiani developed a modified electrospinning apparatus using charged rotating metallic cylinders and a rotating plastic winding tube[34, 67]. Mondal used a rollers driven by a motor and in order to obtain the yarn formation a glass rod was used to manually remove the electrospun polymer from the spinning zone introduced[48]. More recently, Mounthy used an actual wire as a collector and finally the electrospun filament has been detached and therefor used[49]. However, most of the electrospun filament obtained exhibited limits in their mechanical properties and structure, which restrict their use as surgical suture or for tendon and ligament replacement. Moreover, only a limited fraction of published studies has stressed the safety and the performances of these yarns in vitro and in vivo[49].

Suture materials: an overview

Suture materials play an important role in wound repair but also in tendon or ligament repair. Ideally, sutures should provide support until the tissue has regained sufficient strength. When this has been achieved, the suture material should disintegrate in order to prevent further tissue reactions or wound healing and endogenous tissue growth inhibition[3]. Suture material selection should be based on the physical and biological properties of the material, also varies with type and quality of the treated tissue and the healing rate. Technological improvement has offered an increase in the variety of sutures available on the market with more tissue specific applications. Unfortunately, too often selection has been governed by the personal preference and experience of the surgeon and by economic reason[24]. A suture material could be characterized by good handling characteristics, have a good knot security and tensile strength, resistant to shrinkage and cause minimal tissue reaction, easy to sterilize and would not provide medium for bacterial growth[60]. Several considerations, regarding the material properties, the patient status and the tissue to be sutured, should be made to select the best sure material for each surgical situation. There is no single ideal suture material, the general performance is based on physical and biological properties.

Sutures can be classified by several criteria[39]:

- Degradation behavior: absorbable versus non-absorbable
- Composition: natural versus synthetic
- Structure: monofilament versus multifilament

Absorbable sutures undergo degradation within 60 days. Degradation is mediated by hydrolysis, enzymatic digestion and phagocytosis. Absorbable suture materials include: polyglycolic acid, surgical gut, polydioxanone. Non-absorbable suture materials, including nylon, silk, polytetrafluoroethylene, are not significantly degraded after implantation and are used where extended wound support or implant function is required[39]. Natural suture materials tend to evocate a significant inflammatory reaction; thus, the attention has been drawn to synthetic sutures. Monofilament sutures are made of a single stand; these result in lower tissue drag and are relatively more resistant to harboring microorganisms. However, due to the higher bending stiffness and greater memory, great care must be taken in handling and tying

monofilament sutures, because crushing or crimping can lead to undesirable and premature suture failure. Multifilament suture are composed of several filaments, usually twisted or braided together; generally, they have better pliability and flexibility than monofilament, are less stiff and a higher coefficient of friction is created when the suture is passed through tissue. Multifilament sutures are often treated with special coatings to facilitate tissue passage and reduce subsequent tissue damage[39, 60]. Sutures are the most common implants used in surgical and clinical daily practice and understanding the various characteristics of suture materials enables appropriate selection. However, as mentioned, no single suture material is ideal, and compromises must be made.

Chordae tendineae replacement

Chordae tendineae anatomy and ultrastructure

The atrioventricular heart valves (AHVs) regulate the unidirectional flow of blood through the heart chambers by the cyclic opening and closing of soft tissue leaflets. This mechanism is supported by the chordae tendineae (CT). CT are branched anatomical features connecting the free edge of the cardiac valve leaflet with the papillary muscle and prevent leaflet flail into the atria[54]. Chordae are classified according to the role they play in ventricular dynamics. In a morphological study of human cadaveric mitral valve CT, conducted in 2015, Gunnal proposed a six different types of CT classification[33] (**Figure 2**).

- Classification I: According to the origin, *apical pillar* chordae and *basal pillar* chordae.
- Classification II: According to the attachments or connections to the different parts of valve complex, *true chordae* or *false chordae*.
- Classification III: According to the attachment of CT to the mitral valve cusp, cleft or commissure (*cusp* chordae, *cleft* chordae and *commissural* chordae).
- Classification IV: According to the distribution on the free border or to the ventricular surface of the cusp (*first order* chordae or free-zone-marginal chordae, *second order* chordae or *rough zone* chordae).

- Classification V: According to the branching pattern of CT (*straight chordae* or *un-branched* chordae, *branched* chordae or *fan-shaped* chordae, *dichotomus* or *spiral* chordae, *irregular* or *web forming* chordae)
- Classification VI: According to the gross structure of CT (*tendinous*, *muscular* and *membranous*).

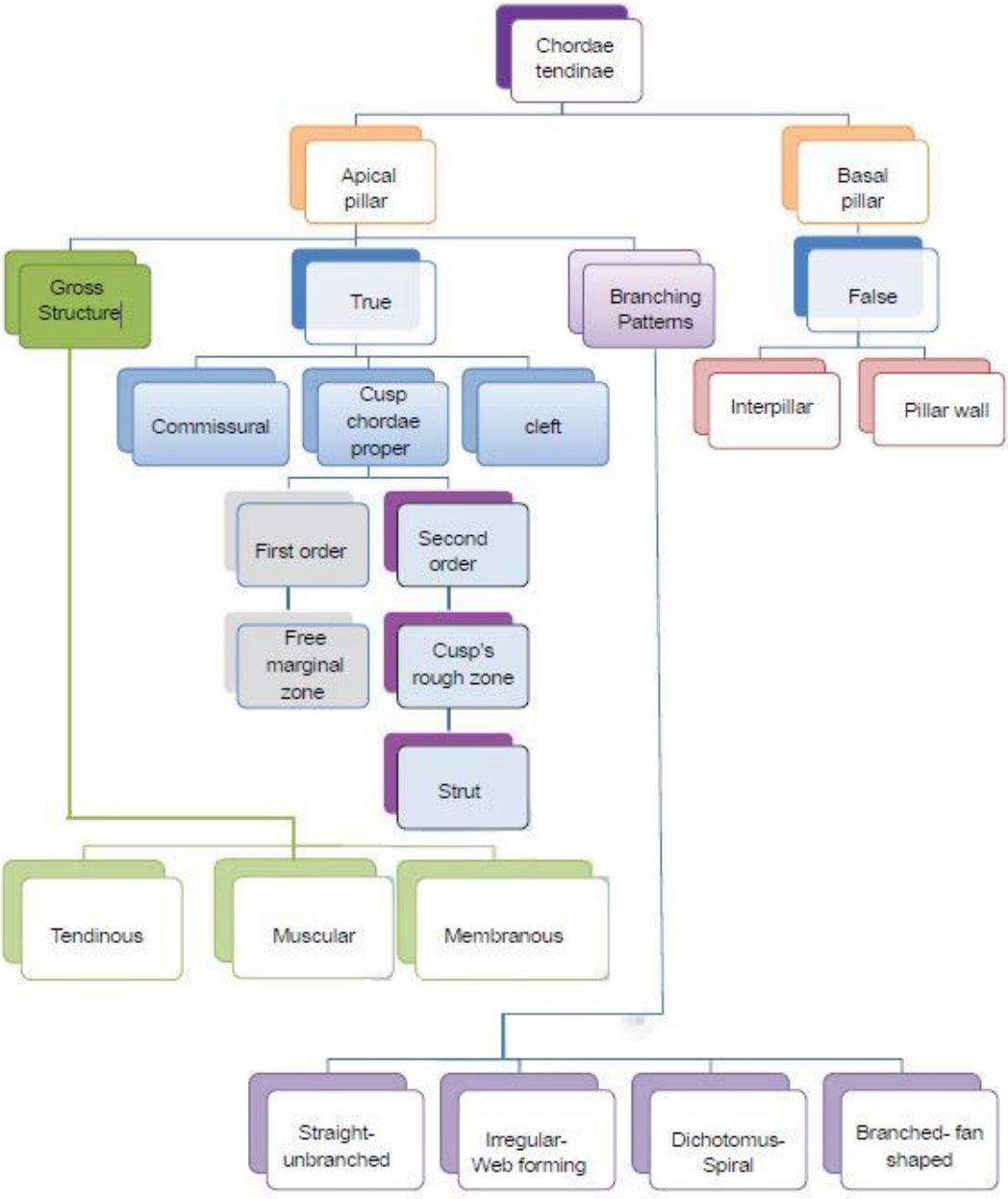

Figure 2 Chordae tendineae classification *by Gunnal et al.*[33]

Previous CT classifications were given by Tandler[61] et al. and later by Quain[1]. However, these classifications divided CT in three orders oversimplifying CT arrangement and morphology and not emphasize morphological differences. The number of links between valve and papillary muscle changes

among individuals, in general consists of 8-12 CT, 1.5-2 cm long and approximately 0.4 mm diameter, approaching the valve leaflet CT divide into thinner branches[46] (**Figure 3**).

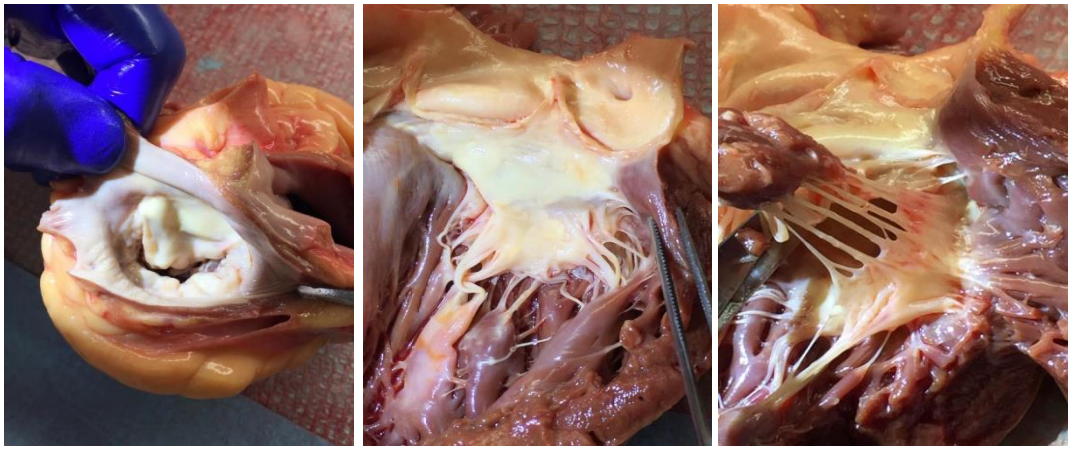

Figure 3 Human mitral valve and sub-valvular apparatus. *Photographs showing cadaveric heart specimen with the ventricular surface and chordal apparatus.*

Millington-Sanders in his work "*Structure of chordae tendineae in the left ventricle of the human heart*" showed the main structural components of CT[46]. CT observed by scanning electron microscopy (SEM) showed an external layer of endothelial cells. On removal of the endothelial superficial layer a pattern of elastic fibers. The interior of the CT showed collagen bundles within linearly arranged dense connective tissue (**Figure 4**).

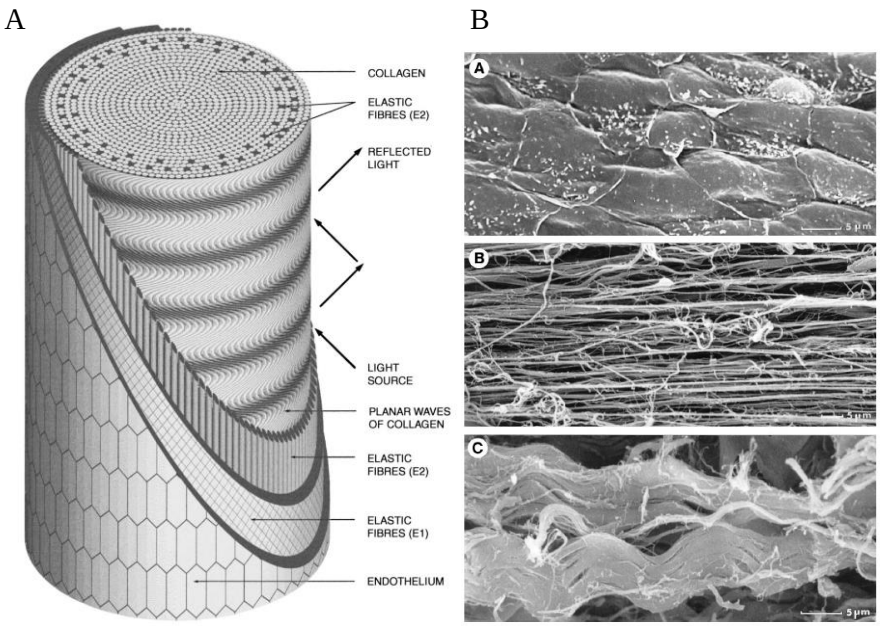

Figure 4 Structure of chordae tendineae. *A) Schematic diagram showing the main structural components of the chorda. B) Scanning electron micrograph of the chorda. Fist picture from the top (A) shows the external aspect of*

the endothelial cells of chordae. Second picture (B) shows the elastic fibers situated underneath the endothelium. Third picture (C) shows interior of a split chorda with waved collagen fibrils[46].

From an ultrastructural point of view, CT are tendinous tissues, consisting of collagen fibrils, proteoglycans, elastin, fibroblasts, and water[42]. Collagen fibrils are the main building block of CT[43], the range of collagen fibril diameter is 40-70 nm, falling in to the lower range of the typical 20-180 nm fibril diameter of tendinous tissue. CT collagen fibrils interacting with glycosaminoglycans (GAGs), GAGs are assembled into a parallel fiber bundles with a sinusoidal crimp pattern. In 2004 Liao and Vesely studied the ultrastructural composition of three order of CT, marginal, basal and strut chordae. The authors compared the main component percentage, water, collagen, GAGs and elastin, among the three CT groups. As previously reported from the same research group [43] the ultrastructures of chordal types are significantly different from each other, this corroborated that each of the three chordal groups had stress relaxation curves that were statistically different. Moreover, using the Verhoeff & van Gieson and the immunohistochemical (IHC) staining, Ritchie et al. showed, in 2005, areas in the CT outer layer where were identified as blood vessels. The vessels were found to run in the longitudinal direction. This indicates that the vessels circled the CT as it proceeded from the papillary muscle to the leaflet[53].

Artificial chordae

As mentioned in the previous paragraph recent studies showed how CT are more than simple collagenous structures, but living tissue that supports and feeds the valve apparatus[53]. These differences in the CT function and structures must be considered during CT replacement as they may be essential in the long-term outcome of the surgical procedures. Elongated or ruptured CT are frequent causes of valve incompetence, in particular mitral valve (MV). In the past, MV regurgitation or prolapse following CT elongation or rupture was performed by valvular replacement[11]. However, during the last thirty years, long-term outcomes of MV replacement encouraged cardiac surgeons to favor repair instead. The overall MV repair goals are restoring valve function and preserve the ventricular function. Due to the complexity of the surgical operation, the procedures to replace, excide, repair, and transpose CT have had variable results. Thanks to the pioneering surgical efforts of Carpentier, Duran, David and many others AHV repair techniques have become quite sophisticated. Material like silk, Teflon, nylon, bovine pericardium and own patient tissue have been used during the years. Unfortunately, there are no

evidences on the long-term performances of these materials. In "*Artificial Chordae"* Tirone David describes his experience of twenty years of CT replacement using expanded polytetrafluoroethylene (ePTFE) suture, commercially available as GoreTex®[25]. CT replacement with ePTFE has become popular since reported in 1985 by Vetter and his group in a sheep model[65]. There is experimental evidence that ePTFE sutures can be used for CT replacement, but despite the prevalence of the procedure, there are still issues such as elongation of artificial CT, rupture of native CT, calcification[54]. The ePTFE is a high molecular weight compound of carbon and fluorine, sutures made of this material are porous and with an electronegative surface, which minimizes interactions with the components of blood flow, reducing thrombogenicity[9]. When implanted the ePTFE CT will, over time, encapsulated by dense fibrous tissue, covered by endothelium, while maintaining normal mechanical function. In 1989, Revuelta reported a scanning electron microscopic view of a ePTFE artificial chorda 24 months after implantation in a sheep[52] (**Figure 5**). During his study 35 sheep were used, five of them died within the first month after the surgery. None of the surviving animals had signs of heart failure or recognizable thromboembolism post-operatively. However, due to the ePTFE porous structure, the artificial chordae

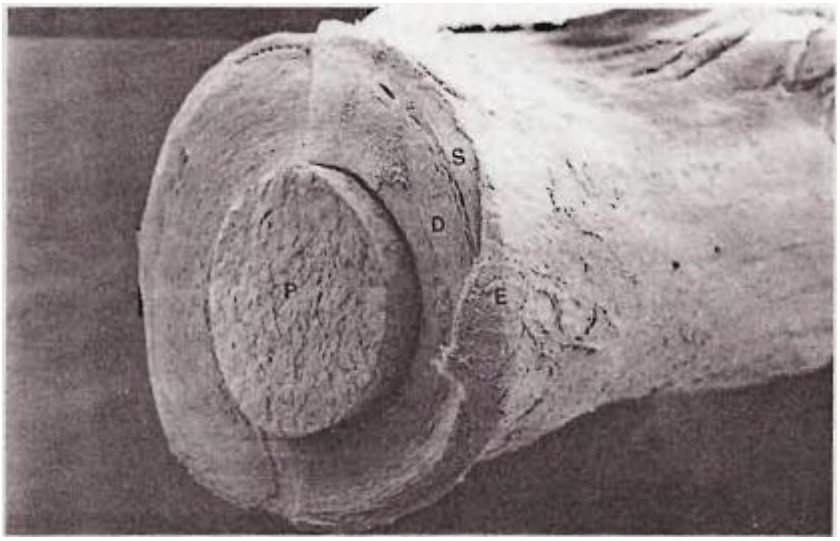

Figure 5 Scanning electron microscopic view of a PTFE suture 24 months after implantation. *A well-organized sheath covers the prosthesis (P). The dense core (D), spongiosa (S), and endothelium (E) are clearly identified*[52].

can become calcified, leading to eventual rupture[9, 16]. Indeed, Caimmi and his group analyzed, in two different studies[10, 11], the mechanical and structural properties of ePTFE artificial CT. In spite the claimed biocompatibility of this material, ePTFE displayed not adequate compliance in long specimen

due to its microporous structure. In particular ePTFE chordae showed higher compliance than native CT and the stiffness of artificial chordae increased with the implant length. Despite the improvement in surgical practice, CT replacement has remained fundamentally unchanged during the last few decades, although is well established that the continuity between papillary muscles and the valve annulus is probably the most important factor in order to preserve the native heart valve function. Future research efforts will concentrate on microstructure of a new generation of artificial CT to reduce the chance of disease-based failure.

Host response to injuries and foreign body

Implanted biomaterials, such as suture materials, are usually recognized as "foreigners" by the host immune system and may elicit a tissue response, usually inflammation, which interferes with wound healing and potentially increases the risk of infection. The permanent or temporary interactions between polymeric fibers and cells regulate the biochemical and genetic cellular activity, influencing the cellular behavior, including phenotype and inflammation response, and modulate the cell adhesion, migration, proliferation and differentiation[63]. The basic stages of wound healing in response to biomaterials are acute inflammation, followed by granulation tissue formation and the foreign body reaction that includes fibrous tissue and contracture. First, tissue injury is characterized by microvascular injury and extravasation of blood into the wound (immediate). Platelets degranulate and release growth factors and chemoattractant. These proteins start the healing cascade attracting and activated monocytes/macrophages to the site of implantation. In an early inflammatory phase (1-2 days) neutrophil granulocytes are the first cells to infiltrate site of injury. Then, in a late inflammatory phase (2-3 days), macrophages start to assemble, to phagocyte bacteria, necrotic tissue and debris and release chemoattractant signals. Blood monocytes undergo a phenotypic change to become tissue macrophages. Starting from this phase, macrophages become the predominant cells population and cause severe alteration in wound healing. About the third day starts the proliferative phase and lasts for up to 4 weeks. Fibroblasts are attracted in the area by chemiotactic factors. Once within the wound, fibroblasts proliferate and produce the matrix proteins fibronectin, hyaluronan and, later, collagen and proteoglycans. These factors will help to remodel the area and will be essential for the repair process.

When an implanted biomaterial is present, fibroblasts surrounded the implant and deposit ECM component. The long-term outcome is the fibrotic encapsulation of the implanted biomaterial. With progression of the proliferative phase, the provisional fibrin/fibronectin matrix is replaced by the newly formed granulation tissue. By 3-5 days, granulation tissue is well established, this phase is characterized by neovascularization and edema. Starting from the first week a continuous synthesis and breakdown of collagen characterize the remodeling phase and the scar maturation. The ECM is constantly remodeled, equilibrating to a steady-state. The remodeling can last up to two years[28, 30, 37, 40].

Macrophage polarization

Implanted biomaterials appear to exert an influence on the host immune response. The role of macrophages in fibrosis is becoming more prominent. Macrophages are monocyte-derived myeloid cells that develop from a common myeloid progenitor cell residing within the bone marrow of adult mammals[31]. Macrophages are a heterogeneous cell population. Upon leaving the bloodstream and migration into sites of inflammation, macrophages become activated in response to signals present in damaged tissue or associated with pathogens[8]. Different functions that macrophages have are controlled by the macrophage phenotype. Broadly, polarized macrophages are referred as M1 or M2 phenotype. Classically activated or M1 macrophages are stimulated by interferon gamma (IFNγ), or tumor necrosis factor (TNF)α and lipopolysaccharide (LPS). In general, M1 macrophages are microbicidal and play a role in cytotoxic host defense. M1 express interleukin (IL) 10, metabolize arginine and produce high levels of inducible nitric oxide synthase (iNOS). In contrast, M2, "alternatively activated", are stimulated by a variety of signals, including IL-4, IL-13 and IL-10. M2 macrophages have high levels of scavenger receptors, produce arginase, are involved in polarized T helper 2 (Th2) reaction, are able to facilitate tissue repair, constructive remodeling through ECM construction and angiogenesis.

AIMS OF THE PROJECT

The overall goal of this project was to develop new methodologies that could be used to optimize electrospun scaffold for tissue engineering application, especially for cardiovascular use. Despite the enormous potential of electrodeposition technique, little effort has been made to fabricate electrospun filaments and yarn. The potential of electrospun filament has been demonstrated for tendon and ligament tissue as they can mimic collagen hierarchical architecture and mechanical properties. However, chordae tendineae replacement for heart valves is still mostly based on conventional suture materials which do not recapitulate the native micro-architecture nor the mechanics, as they do not allow for endogenous tissue formation of functional tissue.

FIRST AIM: Evaluate in vivo and in vitro the biomechanical properties of a continuous electrospun suture wire

Electrospun materials have been investigated for the repair of various biological tissue. Fabricating continuous electrospun filaments is highly attractive because they can be used as biocompatible sutures with tailored mechanical properties and structures. In the present work, PEUU electrospun continuous suture wires with tunable mechanic have been fabricated by a novel mandrel-less apparatus. It was supposed that the direction of fiber deposition could be controlled based on the rotation of the mandrel-less apparatus and that different wire ultra-structures will induce changes in mechanical properties and biological response compared to commonly used suture materials.

SECOND AIM: Evaluate the mechanical properties and the *in vitro* cell growth of biomimetic engineered chordae tendineae

Despite the progress in surgical techniques, chordae tendineae (CT) replacement has remained fundamentally unchanged during the last few decades. The use of common sutures, such as ePTFE, for CT replacement, has demonstrated adequate midterm clinical results; however, the materials utilized do not recapitulate the microarchitecture nor the mechanics of native CT and do not promote tissue regeneration. Moreover, over the years, suture material can be totally covered with calcific fibrous tissue

and cause mechanical stress upon the valvular tissue, de-novo CT rupture, papillary muscle ischemia or rupture. In this work a PCUU biomimetic engineered chordae tendineae (BECT), with a high degree of fiber alignment, have been fabricated, by a novel mandrel-less electrospinning apparatus, in order to mimic the native CT. BECT have been microintegrated with rat fibroblasts to study the cell behavior in a high aligned fibrous scaffold. It was supposed that fiber alignment coupled with mechanical stimuli can improve cell infiltration and growth.

MATERIALS AND METHODS

A CONTINUOUS MICROFIBER WIRE FOR SOFT TISSUE APPLICATIONS

Micro-structured rope-like material apparatus

An explanatory micro-structured rope-like material apparatus schematic is provided in **Figure 6**. The apparatus consists of two motors M1 in tower one and M2 in tower two. Each motor controls the rotation of two mandrels (ω_1 and ω_2) around a common axis and allows start/stop and variable speed rotation. A direct current voltage is necessary for the electrospinning process. The mandrels are connected to an electrically conductive circuit, the voltage generated by the two facing electrodes will induce the deposition of microscopic polymer fibers. The polymer spinneret, connected to a voltage generator as well, is positioned between the two electrodes, polymer flow rate is controlled by a Harvard apparatus. Tower one is also equipped with a third motor (M3) which is responsible for the motion of the spool present in tower one. The third motor and the spool are responsible for the micro fiber-based rope collection: take-up speed and direction can be controlled.

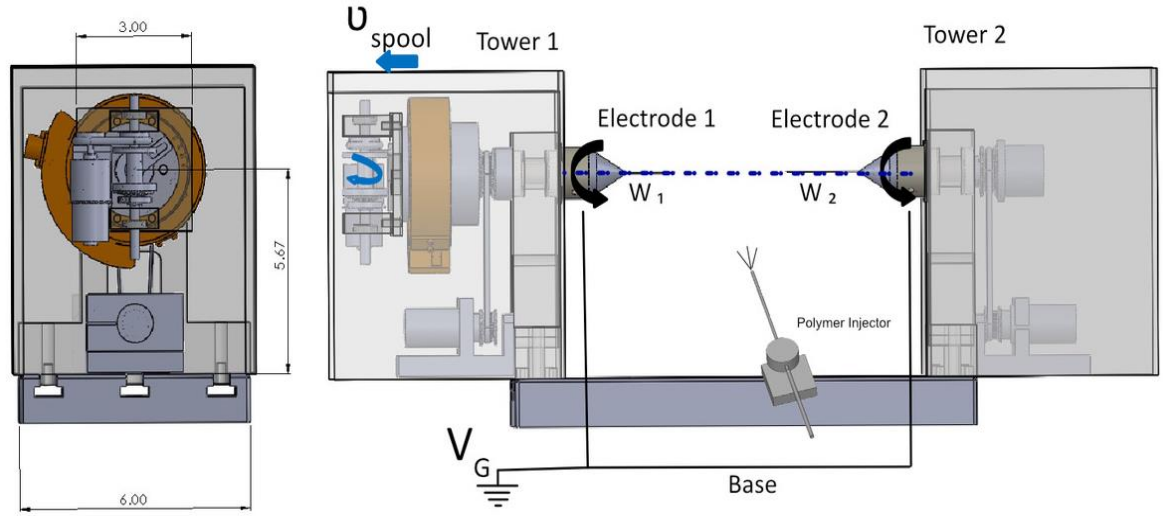

Figure 6 Schematic of micro-structured rope-like material apparatus. *Experimental setup utilized in the study with related fabrication variables. Two high voltage generators control the negative voltage of the two electrodes (VG) and the positive voltage of the polymer (VP). Slits on the base and a moving arm are utilized to set the electrodes and polymer gaps. Motor 1 (M1) in tower 1 controls the rotation of electrode 1 (ω_1), Motor 2 (M2) in tower 2 controls the rotation (ω_2) of electrode 2, the two electrodes spin around a common axis. Tower 1 is also equipped with a third motor (M3) which is responsible for the linear velocity and motion of the spool (v_{spool}). This mechanism is responsible for the collection of the produced rope. The polymer spinneret is positioned between the two electrodes. A Harvard apparatus controls the polymer flow rate. At regimen, the polymer mass introduced in the system via electrospinning is equal to the polymer mass accumulated on the spool. This allows for the continuous production of the micro-fiber-based rope.*

Poly(Esther-urethane)urea micro fiber-based suture wire fabrication

The processing method is based on the notion of mandrel-less deposition, previously introduced in the US patent application PCT/US2018/022863[20], in this study moving electrodes and a rope coiling mechanism are introduced. The Poly(Esther-urethane)urea (PEUU) used for this study was synthetized as previously described[32]. Suture wires used were fabricated by electrodeposition technique, using the developed apparatus described in the previous paragraph. The wire fabrication was conducted as follows. The PEUU polymer was dissolved 12% w/v in hexafluoro isopropanol (HFIP) the day before the wire fabrication. Polymer voltage was 10kV and polymer flow rate was set at 3 ml/h. Electrodes voltage was 2kV, polymer needle-electrodes gap was 5 cm same distance between the two electrodes. Different microfiber depositions were produced by changing the mandrel rotation. Herein described in detail the fabrication of the micro fiber-based rope used for the *in vitro* and the *in vivo* study. For the in vitro study the samples were fabricated as showed in Table 1.

GROUP	MANDREL ROTATION	DEPOSITION TIMES	FINAL DEPOSITION TIME
$\omega_1=\omega_2$	ω1 = 30 rpm - ω2 = 30 rpm	3 minutes	3 minutes
$\omega_1<\omega_2$	ω1 = 0 rpm - ω2 = 30 rpm	3 minutes	3 minutes
$\omega_1>\omega_2$	ω1 = 30 rpm - ω2 = 0 rpm	3 minutes	3 minutes
MULTILAYER 1	ω1 = 30 rpm - ω2 = 30 rpm ω1 = 0 rpm - ω2 = 30 rpm ω1 = 30 rpm - ω2 = 0 rpm	1 minute 1 minute 1 minute	3 minutes
MULTILAYER 2	ω1 = 0 rpm - ω2 = 30 rpm ω1 = 30 rpm - ω2 = 0 rpm ω1 = 30 rpm - ω2 = 30 rpm	1 minute 1 minute 1 minute	3 minutes

Table 1 Electrospun wire fabrication parameters.

For the in vivo study the suture wire was fabricated as follow: during the first step the mandrels ω_1 and ω_2 ($\omega_1=\omega_2$) 30 rpm rotated and the direct current voltage was on, the spool mechanism was not in function, that allowed the first polymer deposition. After 3 minutes the polymer was macroscopically spanned from the two electrodes. The second step was the elongation in which the spool mechanism was in function (υ_{spool} 2 cm/min). A fabrication time of 20 minutes produced a round cross-sectioned

rope of 32 cm in length with a diameter of 0.834±0.248 mm (**Figure 7**A and B). The casted PEUU wire, used as control in this study, was obtained injected 12% PEUU solution in a polytetrafluoroethylene (PTFE) 2.5 mm diameter tube, dried under ambient condition in fume hood 48 hours. The suture wires were sterilized triple washed in ethanol 70% for 15 minutes each and triple washed in Phosphate-buffered saline (PBS) for 15 minutes each, they were then exposed to UV light for 20 minutes.

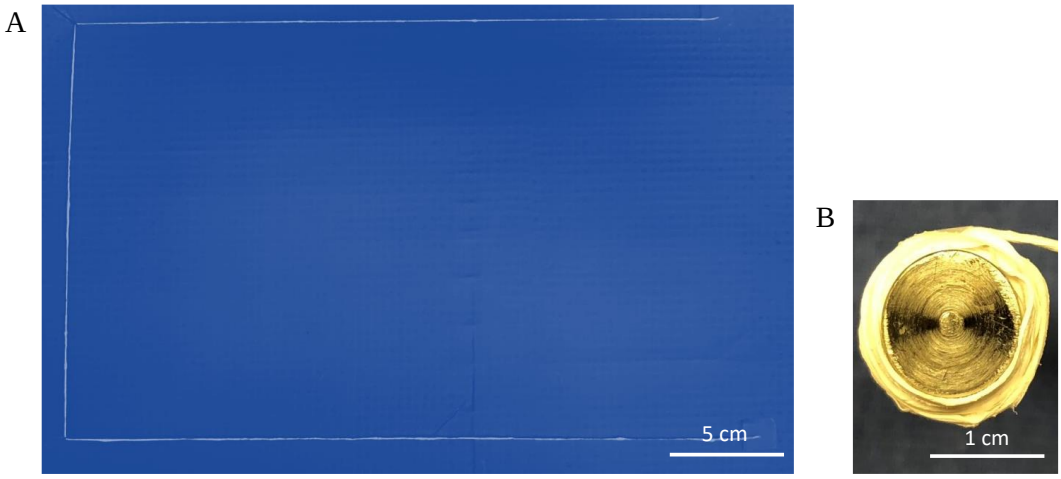

Figure 7 Fabricated micro-structured rope. *A) 32cm wire produced in 23 minutes. Fabrication time: step 1 - 3 min deposition time, step 2 - 20 min elongation time. Fabrication variables for both steps: V_P: 10kV, V_G: -2kV, Flow rate: 3 ml/h, Polymer-Electrodes gap: 5 cm, Electrode gap: 5 cm, $\omega_1=\omega_2$: 30 rpm, v_{spool}: 2 cm/min. B) Electrospun wire spool*

Electric field study

In this work, COMSOL Multyphisics 5.2 software, a finite element software, has been used to analyze the electric field profile during the fabrication. A 2D and 3D geometric models were evaluated. A physics-controlled meshing sequence with a fine mesh resolution was used. The distance between the polymer needle and the electrodes was set at 5cm, the same distance between the two electrodes. Materials were selected from the software library: aluminum for the polymer needle and copper for the electrodes. The environment was set as air. Electric charge conservation and potential voltage on the electrodes and needle were set as boundary conditions.

Scanning electron microscopy and fiber analysis

Surface characteristics of the PEUU ES suture wires were evaluated by scanning electron microscopy (SEM). The samples were sputter coated with 5nm of gold-palladium (Sputter Coater 108 auto, Cressington Scientific Instruments, Cranberry Twp., PA) and imaged using a JEM-6335F scanning

electron microscope (Jeol, USA) at a working distance of 8mm and magnifications of 100X and 1000X (**Figure 8**A). Seven randomly chosen images were selected for each of the three scaffold groups. The sample visual inspection was coupled with a complete fiber network topology quantitative analysis (**Figure 8**B). Fiber diameter, porosity, pore size, orientation index and orientation angle were characterized with a custom-made algorithm developed with MatLab (The Math-Works, Natick, MA)[22].

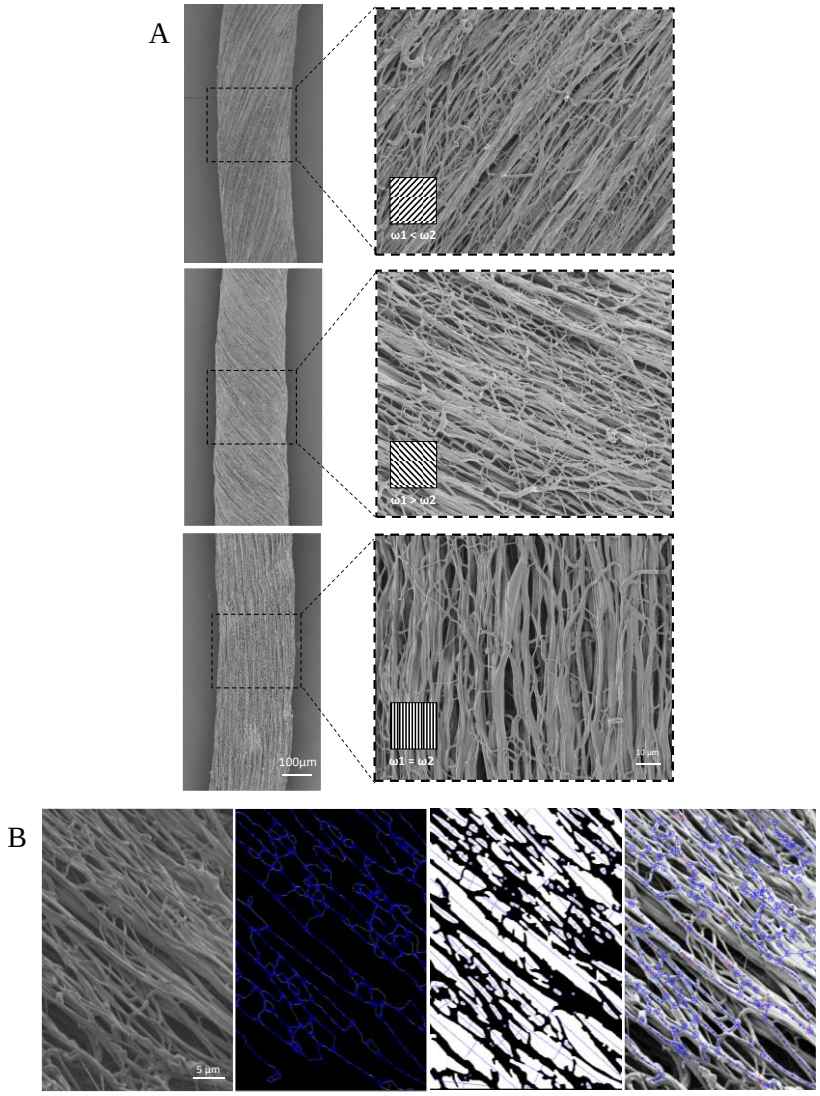

Figure 8 Scanning electron microscopy and fiber analysis. *A) SEM analysis at 1000X magnification. 21 images, 7 per each group, were collected in order to characterize the ES wire ultrastructure. B) Fiber diameter, orientation index, orientation angle, porosity and pore size were characterized using the method of D'Amore, A. et al. 2010*[22]

2D PEUU ES and Cast layer preparation

Electrospun (ES) and Cast layers were used for the in vitro assessment of inflammatory activity evaluation on macrophages and to obtain the degradation products. For ES and Cast layer fabrication PEUU polymer was dissolved 12% w/v in HFIP the day before the layer fabrication. PEUU ES layer

was fabricated as previously described in D'Amore et al.[21]. A steel 114 mm diameter cylinder with rotation speed of 750 rpm and rastering speed of 0.15cm/min was used as a collecting target. The cylinder voltage was kept at -4 kV while rotating. The polymer solution flow rate was 20 ml/h, the needle was at 10 cm by the target and 13 kV charged. The ES layer was fabricated for 20 minutes, the product had an average thickness of 0.04±0.02 mm. The ES layer dried under ambient conditions in a fume hood overnight. PEUU Cast layer was obtained by casting 4 ml of 12% w/v polymer solution onto a clean 13 cm round shaped Derlin® container with flat surface. The layer produced was dried under ambient conditions in fume hood overnight. The product had an average thickness of 0.029±0.007 mm. Finally, the discs used for the in vitro tests were obtained by cutting PEUU ES and Cast layers with a 2 cm diameter punch. The discs were sterilized triple washed in ethanol 70% for 15 minutes each and triple washed in PBS for 15 minutes each, they were then exposed at UV light for 20 minutes.

In vitro accelerated hydrolysis of PEUU ES and cast

PEUU ES and Cast were hydrolyzed using a modification of a previously established accelerated hydrolysis method[47]. PEUU ES and Cast layers, obtained as previously described, were cut in 1x1 cm pieces, weighed, placed in a 50 ml conical tube. The discs were dissolved 6.7% w/v in 3M HCl at 37°C and shook at 50 rpm for 30 days. Solubilized PEUU ES and Cast released by the hydrolysis were neutralized to pH 7.0 with 10M NaOH. The resulting solutions were dialyzed for 24 hours with a 0.1-0.5 kD membrane (Float-A-Lyzer™G2 Dialysis Device, Fisher Scientific). The obtained PEUU degradation products were used to treat the bone marrow-derived macrophages.

Animal and experimental procedures

All procedures were approved by and performed according to the guidelines of the Institutional Animal Care and Use Committee at the University of Pittsburgh. Animals were euthanized in accordance with the guidelines of the American Veterinary Medical Association (AVMA) Panel of Euthanasia. For the experiments, female C57BL/6 mice and female Sprague Dawley rats were used. were used.

Bone marrow-derived macrophages isolation and culture

Primary bone marrow-derived macrophages (BMM) were isolated as previously described[27, 57]. Briefly, female 6 to 8-week old C57BL/6 mice (Jackson Laboratories, Bar Harbor, ME) were euthanized via

CO_2 inhalation and cervical dislocation. Femurs, tibia, and fibula were harvested and washed three times in macrophage complete medium consisting of 10% Fetal bovine serum (FBS) (Invitrogen, Carlsbad, CA), 10% L929 supernatant, 10 mM non-essential amino acids (Gibco, Grand Island, NY), 10 mM 4-(2-hydroxyethyl)-1-piperazineethanesulfonic acid (HEPES) (Gibco), 2 mM L-glutamine (Gibco), 100 U/mL penicillin (Gibco), 100 mg/mL streptomycin (Gibco) and 0.1% β-mercaptoethanol in Dulbecco's Modified Eagle Medium (DMEM) high glucose (Gibco). Complete medium was flushed through the medullary space of harvested bones and cells were collected and used for the following experiments. For immunolabeling studies, BMM were plated at 2 x 10^6 cells/mL into 12 and 6 well plates (Corning), and after 7 days were treated with PEUU degradation products (**Figure 9**). BMM were seeded twice on PEUU ES sterile wires, each time with 20 µl, at 10 x 10^6 cells/mL per scaffold. For immunoblotting studies, BMM were seeded 5 x 10^6 cells/mL onto the surface of 2 cm diameter sterile discs of either PEUU Cast and PEUU ES (**Figure 10**). Medium was supplemented 24h after seeding, BMM were differentiated into macrophages for 7 days at 37°C and 5% CO_2 with media changes every 48 hours.

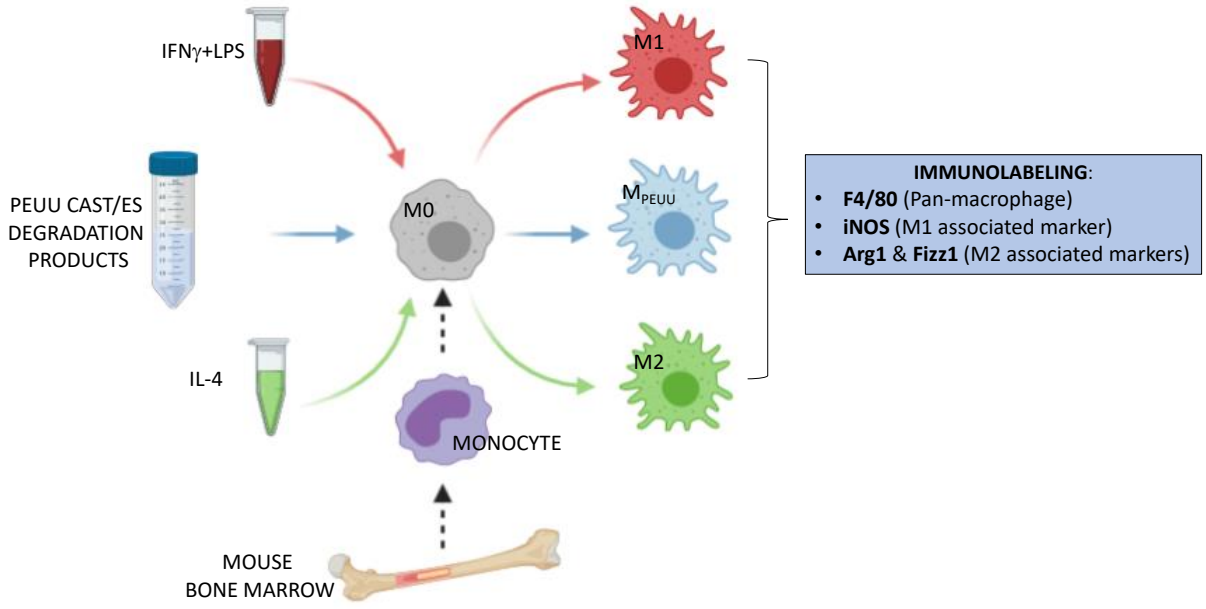

Figure 9 In vitro macrophage response to PEUU degradation products experimental setting.

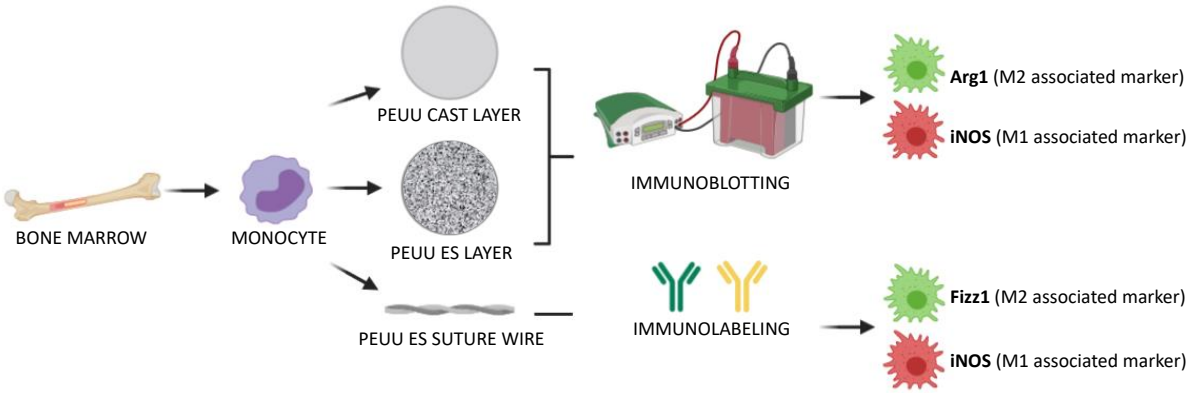

Figure 10 In vitro macrophage response to PEUU 2D and 3D scaffold configurations experimental setting.

Macrophages activation

After 7 days naïve macrophages were stimulated with 1:10 or 1:50 dilutions of PEUU Cast degradation products, or 1:10 or 1:50 dilution of PEUU ES degradation products for the following immunolabeling studies or with 1 ml of the following macrophage activation controls: complete media (M0), 20 ng/ml IFN-γ (Peprotech, USA) + 100 ng/ml LPS (Sigma Aldrich, USA) (M1), 20 ng/ml IL-4 (M2). Treated macrophages were finally incubated for 16 hours at 37°C and 5% CO_2

Immunolabeling of *in vitro* treated macrophages

After 16 hours of incubation stimulated macrophages were washed with PBS and fixed for 20 minutes at room temperature with 4% paraformaldehyde (PFA). PEUU ES seeded wires were collected and fixed in 10% neutral-buffered formalin and embedded in paraffin. Sections of 5 µm were cut and mounted onto glass slides. To prevent non-specific binding, fixed cells and wire sections were incubated in a blocking solution composed of PBS, 0.1% Triton-X, 0.1% Tween-20, 4% goat serum and 2% bovine serum albumin (BSA) for 1 h at room temperature. Blocking buffer was then removed, stimulated macrophages and sections were incubated at 4°C for 16 hours in a solution of one of the following primary antibodies: 1) monoclonal anti-F4/80 (Novus) at 1:200 dilution as a pan-macrophage marker; 2) polyclonal anti-inducible nitric oxide synthase (iNOS) (Abcam, Cambridge, MA) at 1:100 dilution as an M1-like marker, and 3) anti-Arginase1 (Abcam, Cambridge, MA) at 1:200 dilution, as an M2-like marker. Primary antibodies were removed and after PBS washing a solution of fluorophore-conjugated secondary antibodies, Alexa donkey anti-rabbit 488 or Alexa donkey anti-rat 488 (Invitrogen, Carlsbad,

CA), were added to the appropriate well/section for 1 h at room temperature. The antibodies were then removed, the cells were washed with PBS, and the nuclei were counterstained using 4′,6-diamidino-2-phenylindole (DAPI). Cytokine-activated macrophages were used to establish standardized exposure times (positive control), which were held constant throughout groups thereafter. Images of three 20x fields were taken for each well using a Zeus live-cell microscope. CellProfiler (Broad Institute, Cambridge, MA) was used to quantify images.

Immunoblotting of *in vitro* treated macrophages

After 7 days of differentiation, the expression of macrophage activation markers was evaluated on macrophages seeded on discs of either PEUU Cast or PEUU ES and macrophages on tissue culture plastic controls. After 16 hours of induced activation, the treatments were removed, stimulated macrophages and seeded PEUU discs were washed with PBS. Cell seeded in plate were scraped, collected, and centrifuged. PEUU ES and Cast discs were collected in 1ml Eppendorf. Samples were subsequently lysed in radioimmunoprecipitation assay (RIPA) buffer supplemented with protease inhibitor cocktail. Lysates were then quantified using bicinchoninic acid (Bio-Rad). 10 mg total protein in Laemmli buffer containing 5% β-mercaptoethanol were loaded, in a number of 3 biological replicates, to 20% polyacrylamide MiniPROTEAN TGX pre-cast gel (Bio-Rad) and run at 150 V for ~45 minutes in tris-glycine running buffer. Upon completion, wet transfer was performed using polyvinylidene difluoride membranes in tris-glycine transfer buffer with 20% methanol at 350 mAmp on ice. After 45 minutes, membranes were removed from the transfer chamber, washed for 10 minutes in tris-buffered saline, 0.1% Tween 20 (TBST) and blocked for 1h in TBST with 5% bovine serum albumin (Sigma). After blocking, membranes were incubated overnight at 4°C with: 0.1 mg/ml mouse-anti-β-actin (sc-47778, Santa Cruz Biotechnologies, Dallas, TX), 0.1 mg/ml rabbit-anti-arginase 1 (ab91279, Abcam), or 0.1 mg/ml rabbit-anti-iNOS (PA3-030A, Thermo Fisher). Following primary antibody incubation, membranes were washed 3 times in TBST and subsequently incubated for 1h at room temperature with goat-anti-rabbit horseradish peroxidase conjugated antibodies (Dako Affinity Purified; Agilent, Santa Clara, CA) diluted 1:1000 in TBST with 5% BSA. Membranes were then washed 3 times with TBST and incubated in chemiluminescent substrate (Clarity ECL Substrate; Bio-Rad) for 5 minutes and

subsequently imaged (ChemiDoc Touch; Bio-Rad). Acquired images were analyzed using NIH ImageJ (NIH, Bethesda, MD; https://imagej.nih.gov/ij) and all groups were normalized to the appropriate loading control. Densitometry results were averaged across replicates and means were compared.

In vivo studies and surgical procedure

A number of 15 female Sprague Dawley rats, older than 2 months of age, were used for evaluation of host response to suture materials testing, a number of 3 animals per each tested material was used. Briefly, animals were anesthetized using 1-3% inhaled isoflurane until signs of consciousness could not be elicited. The hair overlying the dorsum of the animals was removed, and the animals were placed prone on a warming pad while receiving inhaled isoflurane. The skin was cleansed using Betadine® and ethanol, allowed to dry, and a 2.5 cm incision was made between the scapulae (**Figure 11**). The skin was subsequently closed using two interrupted sutures composed of one of the following materials: Polyglycolic Acid (PGA), Polydioxanone (PDS 2), Polypropylene (PPL), PEUU Cast, or PEUU ES. Animals were survived for 30-days post-surgery and subsequently sacrificed via CO_2 inhalation and cervical dislocation.

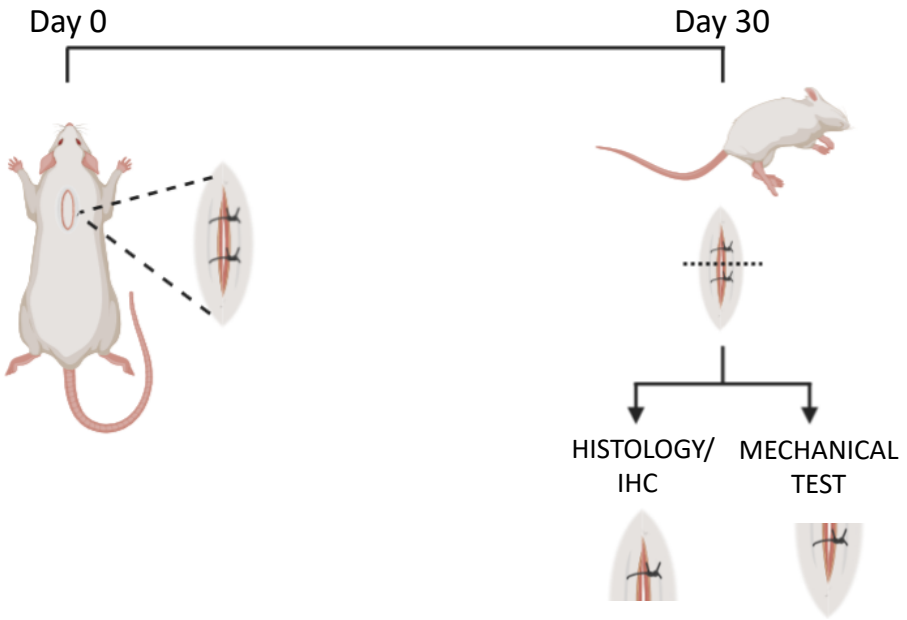

Figure 11 In vivo study experimental setting. *Cartoon representation of the surgical model and macroscopic view of representative sutured incisions. A 2 cm incision was made between the scapulae of each animal following the longitudinal direction (cranial caudal axis). The skin was closed with two interrupted sutures using one of the following materials: PEUU Cast, PEUU ES, PGA, PDS, PPL. A number of 3 animals per each tested material was used.*

Sample preparation

At 30 days we removed the hair from the dorsal skin. Next, an area of 5 x 5 cm section around the treated skin and underlying connective tissue was harvested. The incision was divided in two parts, the upper side was used for the histological and IHC evaluation and the bottom side for the biaxial mechanical evaluation. The suture materials, where present, collected and analyzed by uniaxial mechanical test. The samples for the mechanical evaluation, either uniaxial and biaxial tests, were flash frozen in isopentane cooled in dry ice for 1-minute. Frozen samples were stored at -80°C for 1 week, thawed at 4°C overnight and raised in PBS for 1 hour before testing[14].

Histological evaluation: Masson's Trichrome staining and collagen quantification

Paraffin embedded samples and healthy rat skin controls were transversely sectioned to a thickness of 5μm and stained with Masson's Trichrome in order to evaluate newly formed tissue, cellular infiltration, and scar area. Slides were examined using a Zeus live-cell microscope at 5x magnification. The explant visual inspection was coupled with quantitative measurements. NIH ImageJ software for image analysis was utilized to cut the area among the region of interest identifying the sutured area in the sample images. To assess the foreign body response, a custom-made algorithm, developed in MatLab (Math-Work, Natick, MA), was utilized, as previously described[17], to segment and quantify collagen rich areas. Collagen density was measured under the wound area compared to the rat healthy skin as control.

Immunohistochemical evaluation: immunolabeling and inflammatory host response quantification

Embedded samples and healthy rat skin controls were transversely sectioned to a thickness of 5μm and mounted onto glass slides. Slides were deparaffinized using xylene and ethanol gradients (100-70% EtOH). Immunofluorescence (IF) was performed to assess the macrophage population phenotypes. After deparaffinization, the slides were placed in citrate antigen retrieval buffer (10 mM citric acid monohydrate, pH 6.0), microwaved at 100% power for 45 seconds, followed by 15 minutes at 20% power. The slides were then cooled in copper sulfate solution (10mM $CuSO_4$, 50mM ammonium acetate, pH 5.0) for 20 minutes. Sections were then rinsed three times in TBST solution and then incubated for 1 hour at room temperature in blocking buffer containing 0.1% Triton-X 100, 0.1% Tween, 2% goat

serum, and 1% bovine serum albumin. The blocking buffer was then removed and the sections were incubated overnight at 4°C in a humidified chamber with 1:200 rabbit-anti-CD11b (Abcam), a pan-macrophage marker. Following overnight incubation, each slide was washed in TBST 2 minutes for 3 times. A 1:200 solution of goat-anti-rabbit horseradish peroxidase conjugated secondary antibody (DAKO) in blocking buffer was subsequently applied and microwaved at 40% power for 3 minutes in a humidified chamber and allowed to cool for 2 minutes before washing in TBST. After washing, sections were incubated with a 1:200 solution of red fluorescent horseradish peroxidase substrate (OPAL 570, Perkin Elmer) in 1x Amplification Diluent (Perkin Elmer) for 10 minutes and then washed in TBST. To remove anti-CD11b and anti-rabbit antibodies, sections were subjected to a second round of antigen retrieval in citrate antigen retrieval buffer, followed by cooling copper sulfate solution, and blocked as described above. For each slide, one section was incubated with a 1:200 solution of rabbit-anti-iNOS antibody (Invitrogen) in blocking buffer, and one section was incubated with a 1:200 solution of rabbit-anti-RELMα (PeproTech). Slides with the primary antibodies were then placed on a raised water bath and microwaved at 40% power for 3 minutes, followed by 2 minutes of cooling. Slides were then washed in TBST solution and a 1:200 solution of goat-anti-rabbit horseradish peroxidase conjugated secondary antibody was placed on the sections. Slides with secondary antibody solutions were then placed in the water bath and microwaved at 40% power for 3 minutes, followed by 2 minutes of cooling. After cooling, slides were washed in TBST and a 1:200 solution of green fluorescent HRP substrate in 1x Amplification Diluent (OPAL 520, Perkin Elmer) was placed over each section and incubated in a dark humidified chamber for 10 minutes at room temperature. The sections were then washed in TBST, DAPI nuclear counterstain for 5 minutes. The sections were washed with TBST and subsequently mounted for imaging by fluorescence microscopy.

Uniaxial mechanical test

All the uniaxial tensile tests were performed on MTS Insight® Electromechanical Testing Systems with a load cell of 100N. Samples were tested following the D2256/D2256M *Standard Test Method for Tensile Properties of Yarns by the Single-Strand Method*. Briefly, samples were subjected to 0.75 N preload and strained at a speed of 25 mm/min until failure to determine the complete stress/strain curve.

Before the uniaxial tests, the sample diameters were measured using a Zeiss Microscope System. The PEUU wires, Cast and ES with different fiber arrangement, were tested 24 hours after the fabrication. The suture materials used for the *in vivo* study were tested before and immediately after the sacrifice. Rat dorsal skin between the scapulae was collected from 2 animals as control. The skin was cut with a dog bone-shaped punch, 2 samples were collected from each animal. Samples were cut in the longitudinal direction, parallel to the spine.

Biaxial mechanical test

In order to determine mechanical properties of rat skin, a custom-built planar biaxial stretching system was used. Samples were cut in a square shape, 10 x 10 mm, that contain the sutured area. Prior to mounting the samples for biaxial testing, we carefully removed the subcutaneous layer and any remaining panniculus carnosus. Markers were placed on the corners of a squared area at the center of the sample and used to measure the deformation gradient tensor. Tests were performed using a Lagrangian equi-stress control protocol and a maximum load of 250 kPa[14] was adopted to induce physiologically relevant strain levels. Samples were preconditioned and then tested for 10 cycles of 15 seconds in PBS at room temperature. Data processing was performed, as previously described[21], with a custom-made software developed in MatLab using the free float position of the markers following preconditioning as a reference.

Statistical analysis

Statistical analyses were performed using SigmaPlot version 14.0 (Systat Software Inc., Chicago, IL, USA) and GraphPad Prism version 8 (GraphPad Software, La Jolla CA, USA). The mean value differences between groups were determined by paired T-Test or one-way analysis of variance (ANOVA), for data with normal distribution, and whether the differences were significant, with a post-hoc Tukey HSD (honestly significant difference) test. Otherwise, Welch ANOVA and Brown-Forsythe test, and whether the differences were significant, Dunnett's T3 or Student-Newman-Keuls post hoc test were used. All data are presented as mean ± standard error of mean. Significance level was set at $p < 0.05$.

BIOMIMETIC ENGINEERED CHORDAE TENDINEAE

Mandrel-less electrodeposition apparatus

Figure 12 A and B provide images of novel electrodes set, introduced in the US patent application PCT/US2018/0228633, used to fabricate high-aligned micro-fiber based BECTs. The voltage generated by the two facing electrodes will induce deposition of highly aligned microscopic fibers which macroscopically will span from the left electrode to the right electrode during the electrodeposition. The typical sequence for fibers deposition is illustrated in **Figure 12** A and B, in which is possible to see the fiber deposition. An example of PCUU BECT is provided in **Figure 12**C.

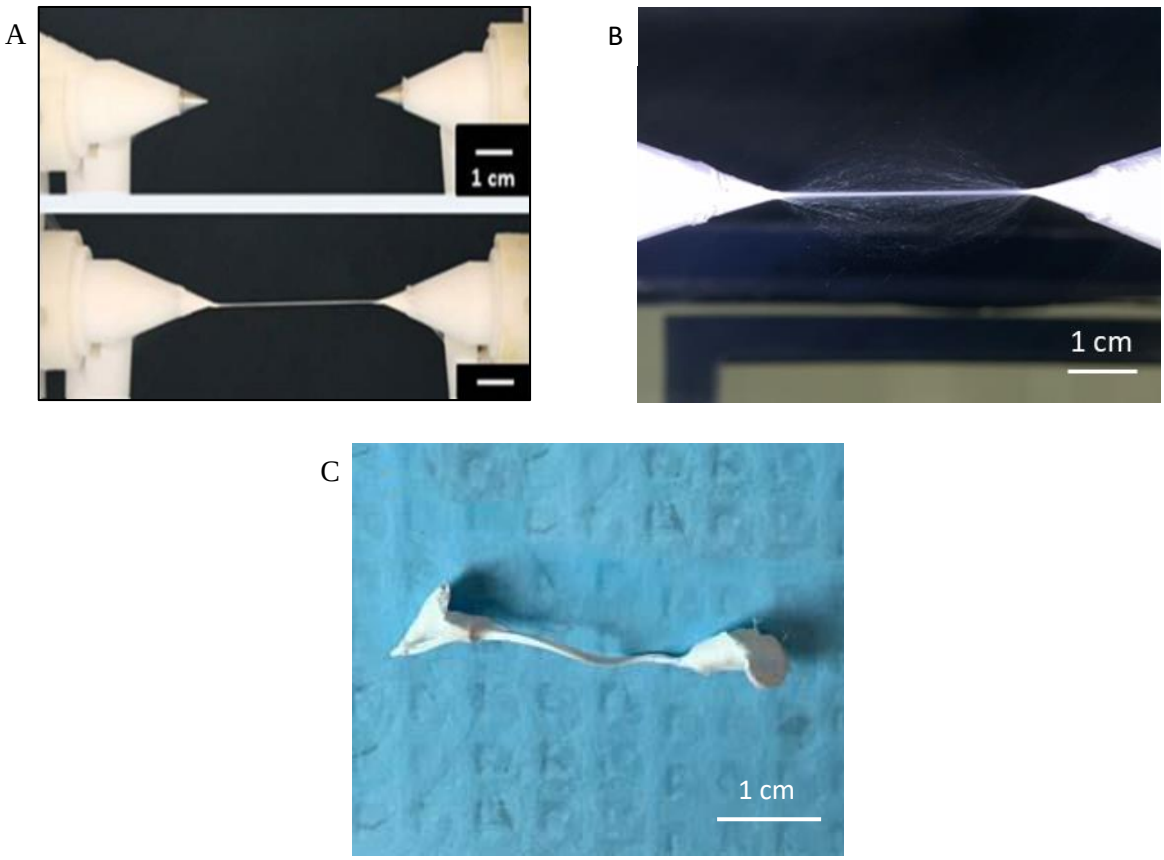

Figure 12 Bioengineered chordae tendineae fabrication process. *A) Mandrel-less electrodes side view: core and stem made of Delrin to shield the voltage field acting on the electrodes and BECT deposition. B) Microfiber deposition process during BECT fabrication. C) Macroscopic view of PCUU BECT.*

NIH-3T3 cell culture

NIH-3T3 rat fibroblasts were obtained from the ATTC® (Manassas, VA, USA). Cells were cultured in tissue flasks (Nunc™, TripleFlask™ Treated Cell Culture Flasks), using DMEM (ThermoFisher Scientific) with 10% of FBS (ThermoFisher Scientific) and 1% of anti-biotic/anti-mycotic (ThermoFisher Scientific) solution and maintained in a humidified atmosphere containing 5% CO_2 at 37°C. NIH-3T3 cells were cultured until they reached approximately 80% confluency before the subculture.

Biomimetic engineered chordae tendineae fabrication

The BECTs used in this study were fabricated by electrodeposition technique, using the electrodes set introduced in the previous paragraph. BECTs were fabricated using PCUU, synthetized as previously described[36], dissolved at 12% w/v in HFIP. The experimental setting used is shown in **Figure 13**A. PCUU electrospinning was accomplished from a capillary charged at +7 kV and located at 12 cm from the mandrel-less electrodes, the electrodes were charged at -7 kV. NIH-3T3 micro-integration was obtained with concurrent electrospraying of a cell suspension. The electrospraying of NIH-3T3 during electrospinning was accomplished by feeding 10 x 10^7 cells/ml at 250 µl/min into a sterilized capillary charged at +7 kV and located at 7.5 cm from the electrodes. After 5 minutes of electrospinning and electrospraying, the micro-integrated BECT were removed from the mandrel-less and placed in static culture media for 72 hours before being divided in three different conditions **Figure 13**B:

- static culture in a plate;
- static culture in tension;
- dynamic culture in a stretch bioreactor.

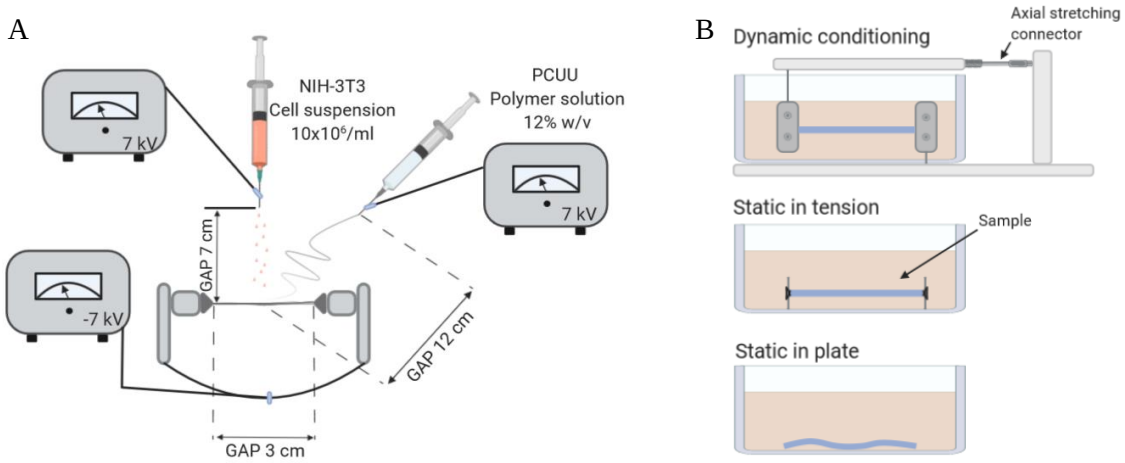

Figure 13 Schematic of microintegrated BECT fabrication and tested conditions*. A) Experimental setup utilized in the study with related fabrication variables. Two high voltage generators control the negative voltage of the two electrodes and the positive voltages of polymer and cell suspension. Two Harvard apparatus control the polymer and the cell suspension flow rate. B) Schematic of the tested conditions.*

Scanning electron microscopy and fiber analysis

Surface characteristics of dry and microintegrated BECTs were evaluated by SEM, as previously described for PEUU ES suture wires. Briefly, samples were sputter coated with 5nm of gold-palladium and imaged using a JEM-6335F SEM at a working distance of 8mm and magnifications of 1000x. Three images were selected from random locations of each sample. Sample visual inspection was coupled with a fiber network topology quantitative analysis. Fiber diameter and orientation index were characterized by a custom-made algorithm developed with MatLab[22].

Stretching bioreactor

The bioreactor used in this study (**Figure 14**) was similar to that previously used by D'Amore[19] and Merryman[45] in their studies. Modifications were made to update the system enabling the test of BECTs samples in dynamic conditions. Motion control was conducted through custom Labview software (National Instruments, NI) with an individual stepper motor controller. The computer connected to the stepper motor controller drives a linear actuator passing through the chamber wall. The linear actuator has two orthogonal cross bars with exiting holes into which stainless steel pins are inserted. The BECTs were fixed with stainless steel clamps and inserted into the stretch bioreactor. For this study, two tween chambers were used. Each chamber was divided into 8 separate wells in order to avoid contamination.

In each well 5 ml of complete DMEM was added and changed every 48 hours The response of the BECTs dynamic group was investigated at 1Hz cycle and 30%[29] of strain for 7 days.

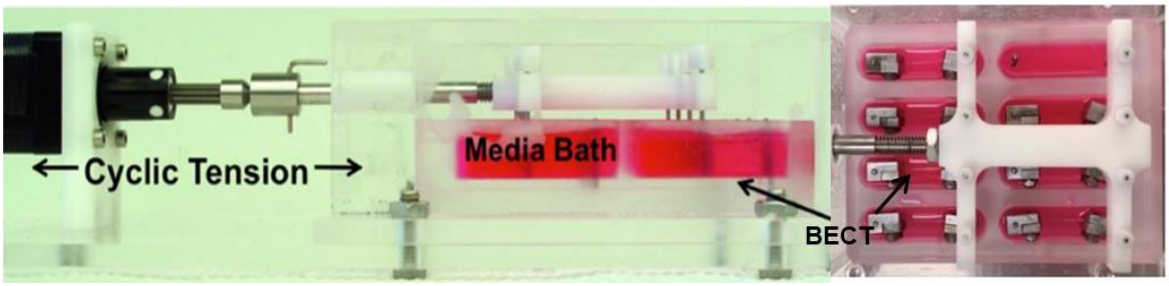

Figure 14 Stretch bioreactor. *Stretch bioreactor loaded with BECT. Figure adapted by D'Amore et al. 2016*[19]

Histological evaluation: Hematoxylin and Eosin

After 7 days of treatment, BECTs were harvested and divided for the following tests. Histological evaluations were carried out on dedicated samples. Samples were fixed overnight, at 4°C, in a mixture of 1:1 glutaraldehyde 2% and complete DMEM and finally embedded in paraffin. Serial sections were stained with Hematoxylin and Eosin (H&E), the staining is based on the ability of the two dyes to differentiate many structures, due to the chemical diversity and affinity for the endocellular elements. The H&E staining was employed to inspect the samples for cell presence and cellular morphology.

Uniaxial mechanical test

Sample diameters were analyzed through the use of a brightfield microscope (Zeiss Microscope System) in 5 different points for each sample. Uniaxial tensile tests have been conducted through an MTS Insight® Electromechanical Testing Systems with a load cell of 100N. Tests have been performed following the standard D2256/D2256. The strain at rate was established at 1 mm/min until failure in order to determine the complete stress/strain curve. For each sample were determined initial modulus, strain at break and ultimate tensile strength by a custom-made MatLab algorithm.

Statistical analysis

Statistical analyses were performed using SigmaPlot version 14.0 (Systat Software Inc., Chicago, IL, USA). The mean value differences between groups were determined by ANOVA followed by a post-hoc Tukey HSD test. All data are presented as mean ± standard error of mean. Significance level was set at $p < 0.05$.

RESULTS

BIOMECHANICAL ASSESSMENT OF A CONTINUOUS MICROFIBER WIRE

Electric field evaluation

Finite element analysis of the suture apparatus electric field was conducted: 2D and 3D models were realized using COMSOL Multiphysics. The modeling results in **Figure 15** show the electric field lines, whose mapping color is based on voltage intensity, guiding the mandrel-less deposition process. More to the point, for the sake of clarity in the 3D visualization, only the electric field lines departing from the central hollow zone of the needle were plotted, whereas in the 2D model a uniform distribution was chosen. As experimentally observed, positively charged polymer flows from the needle, following the oriented electrostatic path towards the electrodes.

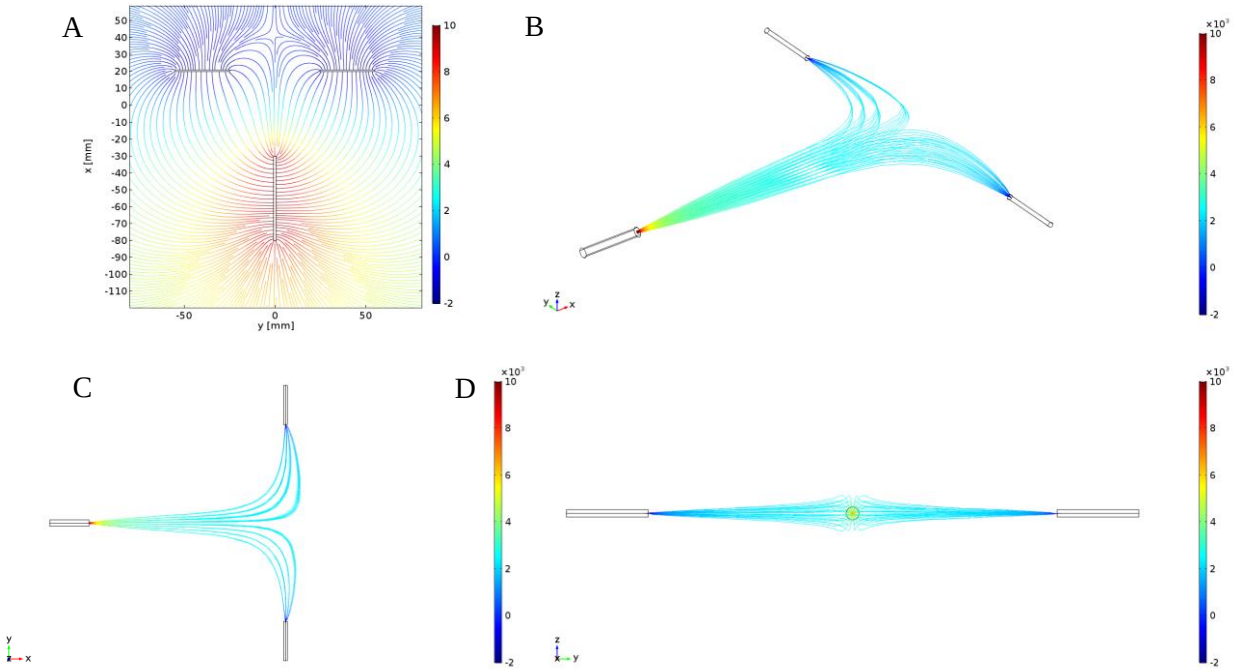

Figure 15 2D and 3D modeling of electric field. *Modeling of the electric field with COMSOL Multiphysics 5.2. Electric field lines, uniformly distributed, departing from the polymer needle and direct to the electrodes. Mapping color is based on voltage intensity. The simulation confirms the experimental results. Electric charge conservation and potential voltage on the electrodes and needle were set as boundary conditions. A) Electric field lines, uniformly distributed, along the working plane - 2D FEM analysis. B) Electric field line departing from needle hole in isometric view – 3D FEM analysis C) Electric field line departing from needle hole from top view – 3D FEM analysis. D) Electric field line departing from needle hole from view – 3D FEM analysis.*

Scanning electron microscopy and scaffold surface characterization

Suture wire surface characterization and quantitative analysis of fiber deposition have been conducted. SEM qualitative evaluation showed different fiber arrangements how can be seen in **Figure 16Figure 16**. Orientation index showed consistency with the known fiber alignment-electrode rotation relationship. The orientation angle drastically changed based on the utilized electrode rotation **Figure 17**B. However, despite the different fabrication conditions, fiber diameter, pore size and porosity remained consistent among the three groups (**Figure 17**C, D and E).

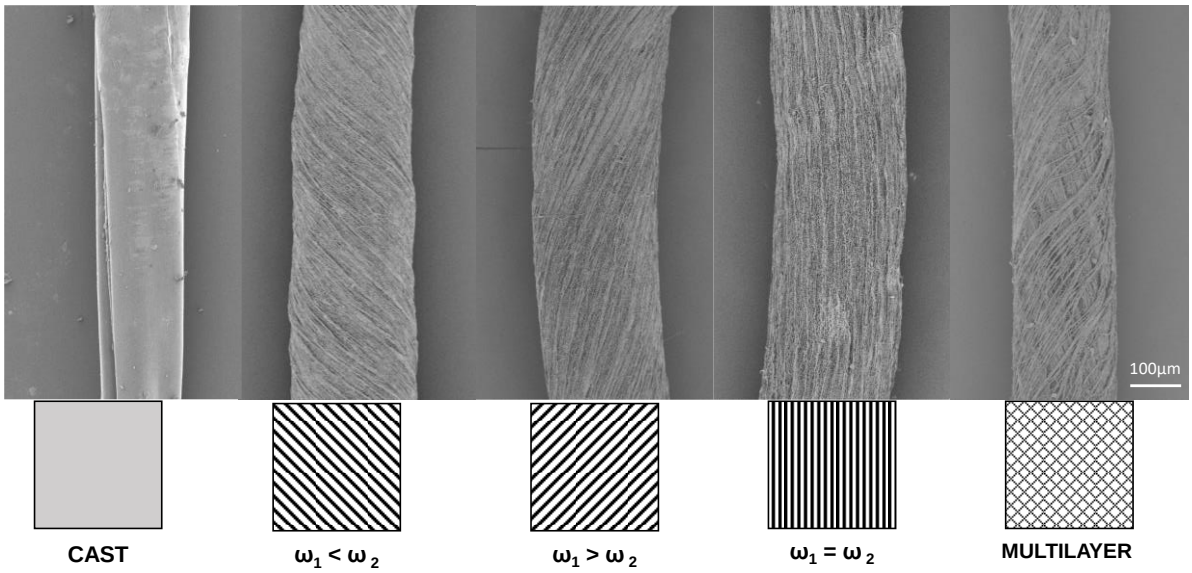

Figure 16 Scanning electron microscopy analysis of different configurations of electrospun suture wires. *The ratio between the rotational speeds of the two electrodes dictates a different fiber arrangement. A multi-layer composite rope can be formed by combining two or more fiber deposition configurations in sequence. Common fabrication variables between all groups: VP: 10kV, VG: -2kV, Flow rate: 3 ml/h, Polymer-Electrodes gap: 5 cm, Electrode gap: 5 cm. Specific fabrication variables in each group are showed in Table 1. 100X magnification was used for image acquisition.*

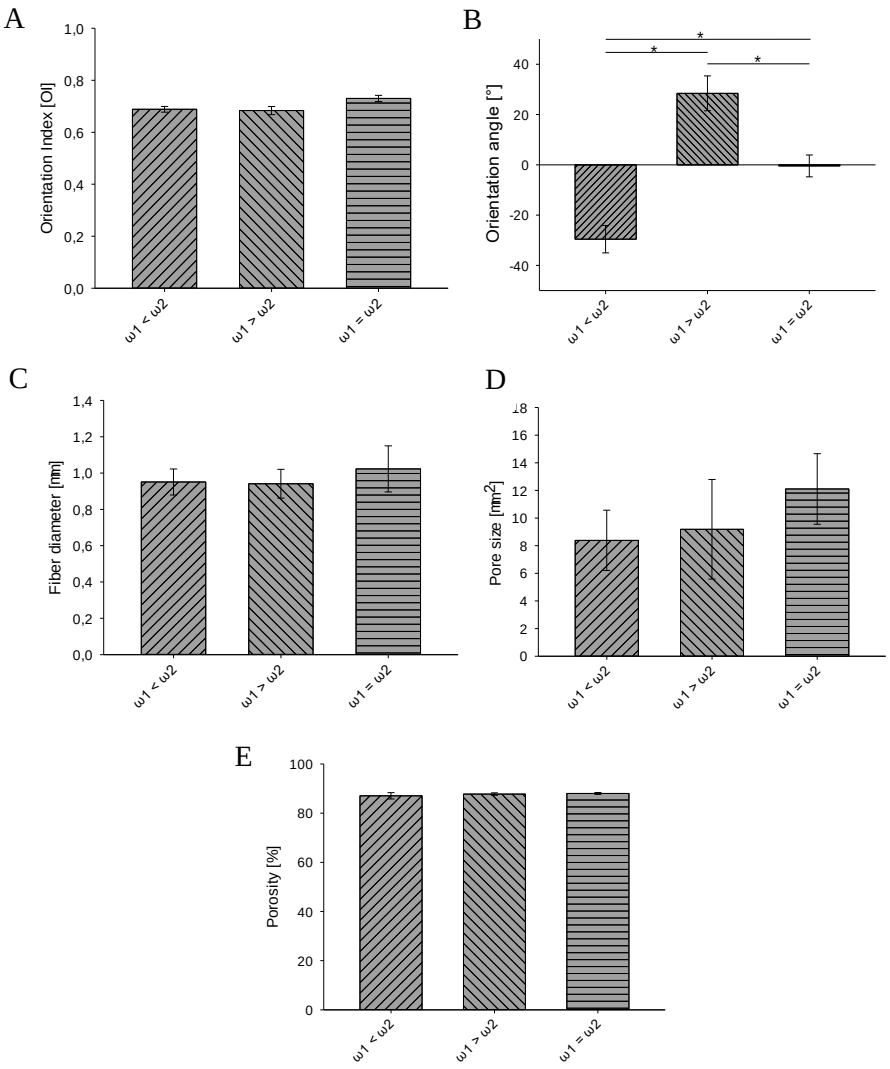

Figure 17 Fiber analysis of electrospun wires. *A) Orientation index. The fiber orientation shows the influence of specific manufacturing parameters. Orientation index showed consistency with the known fiber alignment-electrode rotation relationship. B) Orientation angle. Orientation angle is* cos^2 *Orientation index. Provides further evidence of different manufacturing characteristics. C) Fiber diameter. One Way ANOVA statistical test showed no significant differences among the groups. D) Pore size and E) Porosity did not show any statistical difference and remained consistent among the three groups*

Diameter range and mechanical response

Figure 18A shows the microfiber suture wire cross-section diameter versus the deposition time. The red area indicates the diameter range of suture wires currently available on the market. For each of the three different time point, at 2, 3 and 4 minutes, a number of five samples were fabricated using the following variables: polymer voltage = 10kV, ground voltage = -2kV, flow rate = 3 ml/h, polymer needle-electrodes gap = 5 cm, electrode gap = 5 cm, electrode rotation = 30 rpm $\omega_1=\omega_2$. The sample diameters were evaluated from five random locations of each sample using a Zeiss Microscope System. In **Figure 18**A can be seen that wire diameter increases with deposition time at constant fabrication variables.

Uniaxial mechanical properties of different suture wire fiber deposition were evaluated (see **Figure 18**B). Samples fabrication was conducted as previously described in the materials and methods section (see **Table 1**). A number of four samples per each group was tested. The statistically significant differences show the capacity to modify the rope uniaxial mechanics by changing the fiber arrangement while delivering the identical polymer mass during the deposition process.

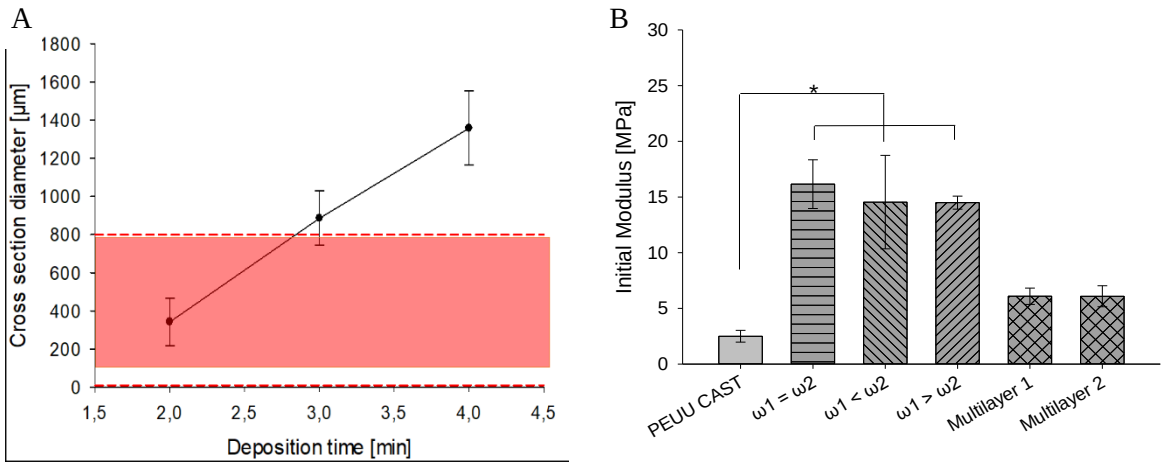

Figure 18 Electrospun suture wire mechanical properties. *A) Diameter versus fiber deposition time. Fabrication variables: VP: 10kV, VG: -2kV, Flow rate: 3 ml/h, Polymer-Electrodes gap: 5 cm, Electrode gap: 5 cm, ω1=ω2: 30 rpm. 5 samples were fabricated for each time point: 2, 3 and 4 minutes. The red area indicates the diameter range of suture products available on the market. B) PEUU control and ES wire initial modulus. Uniaxial tensile test results show the capacity to modify the wire mechanical properties by changing the fiber arrangement while delivering the identical polymer mass during the deposition process. One Way ANOVA shows statistically significant differences among the groups. * = $p < 0.05$.*

In vitro evaluation of PEUU degradation products on macrophage response

Phenotypic profile of murine BMM was determined by immunolabeling via the expression of pan-macrophage marker F4/80, M1-like pro-inflammatory marker iNOS or M2-like anti-inflammatory markers Arginase1 and Fizz1 (**Figure 19**A). Known factors that are promoters of pro-inflammatory (100 ng/ml LPS and 20 ng/ml IFN-γ) or anti-inflammatory (20 ng/ml IL-4) phenotypes were included as controls. Exposure of macrophages to PEUU ES degradation product 1:50 showed a decrease in the number of cells expressing iNOS ($p < 0.05$) (**Figure 19**B, iNOS bar chart) compared to the other treatments. The PEUU ES degradation products 1:10 increased ($p < 0.05$) the percentage of cells expressing Fizz1 when compared to the PEUU ES degradation products 1:50. PEUU Cast degradation products 1:50 showed a decrease in the number of cells expressing the same marker compared to the other treatments (**Figure 19**B, Fizz bar chart).

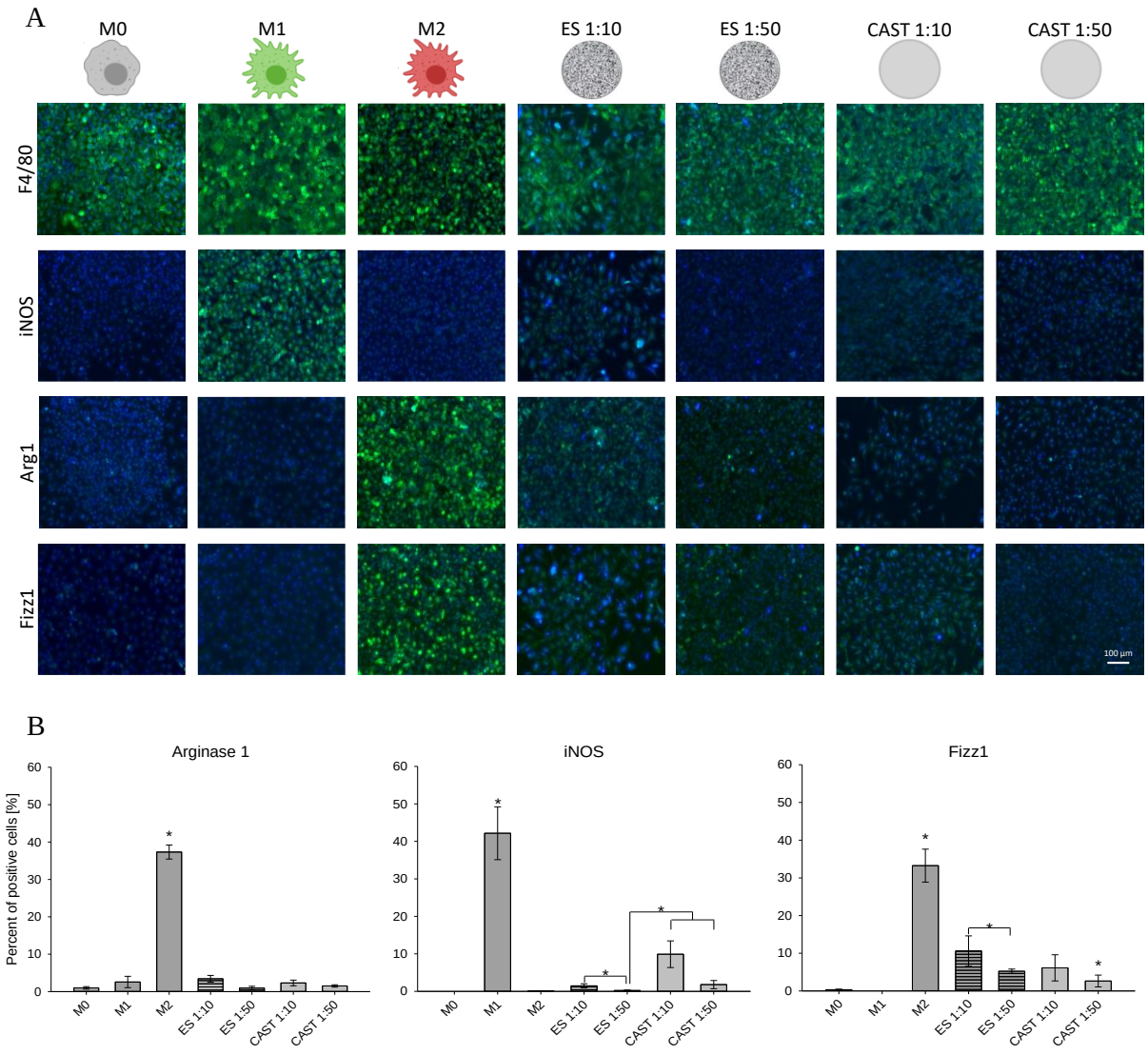

Figure 19 In vitro macrophage response to PEUU degradation products. *A) Activated macrophages phenotype evaluated by immunolabeling. Activation of markers associated with pro-inflammatory (iNOS) and anti-inflammatory (Fizz1 and Arginase1) phenotype was evaluated by immunolabeling. A general marker of macrophages (F4/80), was used. Known factors that are promoters of pro-inflammatory (100 ng/ml LPS and 20 ng/ml IFN-γ) or anti-inflammatory (20 ng/ml IL-4) phenotypes were included as controls. B) Quantification of the response of treated macrophages. Images were quantified using Cell Profiler image analysis software. Differences between stimuli for each marker were evaluated using non-parametric ANOVA test. One Way ANOVA shows statistically significant differences among the groups.* * *= p < 0.001.*

In vitro evaluation of PEUU ES and Cast 2D scaffolds and PEUU ES suture wire on macrophage response

Protein expression of murine BMM on PEUU ES and Cast 2D scaffold and PEUU ES suture wire was determined by western blot and immunolabeling. The expression of M1-like pro-inflammatory marker iNOS and M2-like anti-inflammatory markers Arginase1 and Fizz1 was evaluated. BMM seeded on PEUU ES and Cast 2D scaffolds induced Arginase 1 and iNOS expression (**Figure 20**A). However,

BMM seeded on PEUU ES scaffolds showed enhanced Arginase1 expression when compared with the PEUU Cast ($p < 0.05$). There were no statistically significant differences between the two groups in iNOS expression (**Figure 20**B). The western blot results were also corroborated by the suture wire immunolabeling. **Figure 20**C shows the immunolabeling quantitative analysis on PEUU ES suture wire. The percentage of positive macrophage for iNOS and Fizz was evaluated using CellProfiler and significant changes were observed. A significant change was observed in the number of M2-like macrophages expressing Fizz1 when compared with M1-like macrophages expressing iNOS (**Figure 20**D).

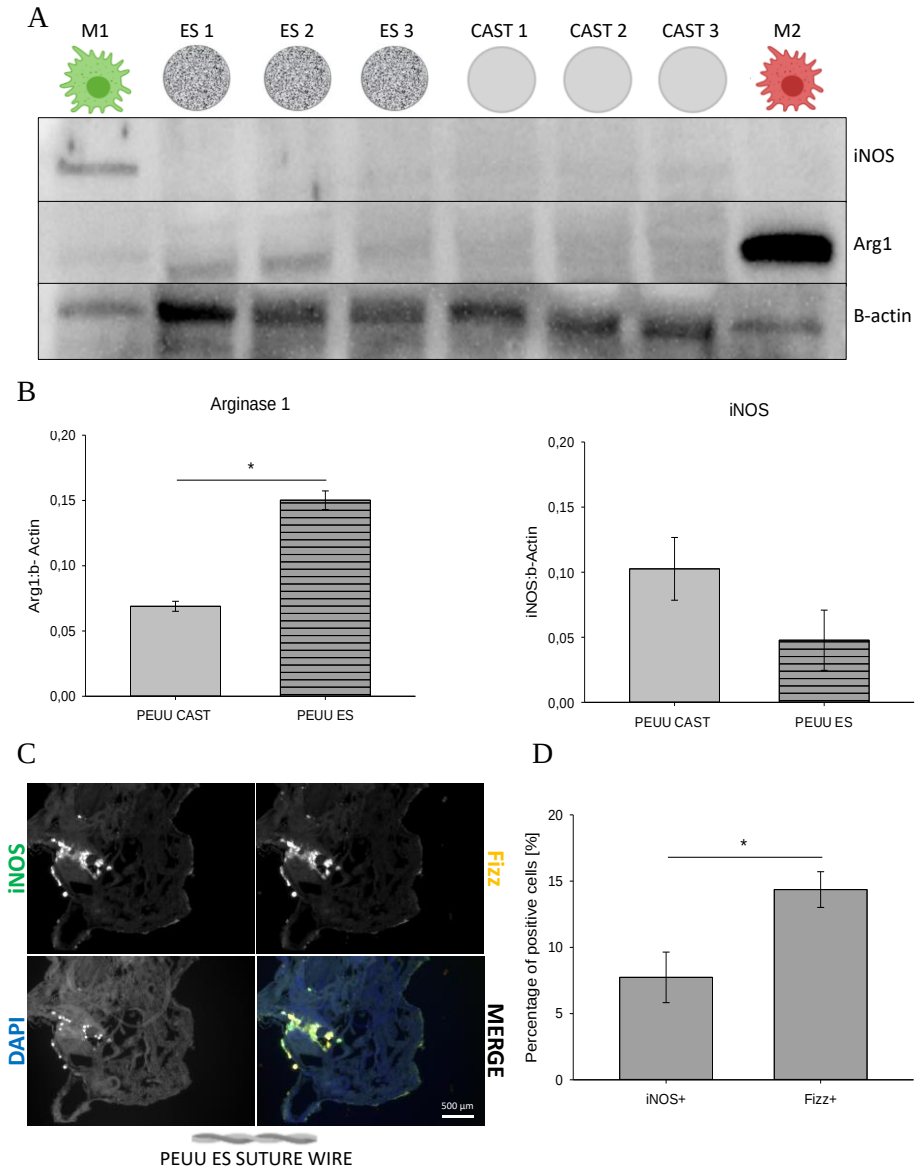

Figure 20 In vitro macrophage response to PEUU 2D and 3D scaffolds. *A) Western-Blot analysis of iNOS and Arginase expression. Bone marrow-derived macrophages were seeded on PEUU ES and Cast 2 cm of diameter*

*discs. After 7 days the samples were collected and lysed in RIPA buffer. Samples were charged in triplicates on the same gel. Western-blot membrane were incubated with anti β-actin, anti Arginase1 and anti-iNOS. B) Immunoblotting quantitative results. Bar charts show the densitometry quantification of pro-and anti-inflammatory protein expression iNOS and Aginase1 normalized to the β-actin. One Way ANOVA test showed statistically significant differences between means. * = $p < 0.05$. C) PEUU ES wire immunolabeling qualitative evaluation. D) PEUU ES wire immunolabeling quantitative analysis. Bar chart shows the percentage of macrophages quantification of pro-and anti-inflammatory protein expression iNOS and Fizz normalized to the total nuclei number. One Way ANOVA test showed statistically significant differences between means. * = $p < 0.05$.*

Ex vivo collagen remodeling assessment

Collagen remodeling assessment of 30 days explant was performed with Masson's Trichrome staining.

The wound healing among the groups was macroscopically evaluated daily and recorded at day 0, 14 and 30 (**Figure 21**).

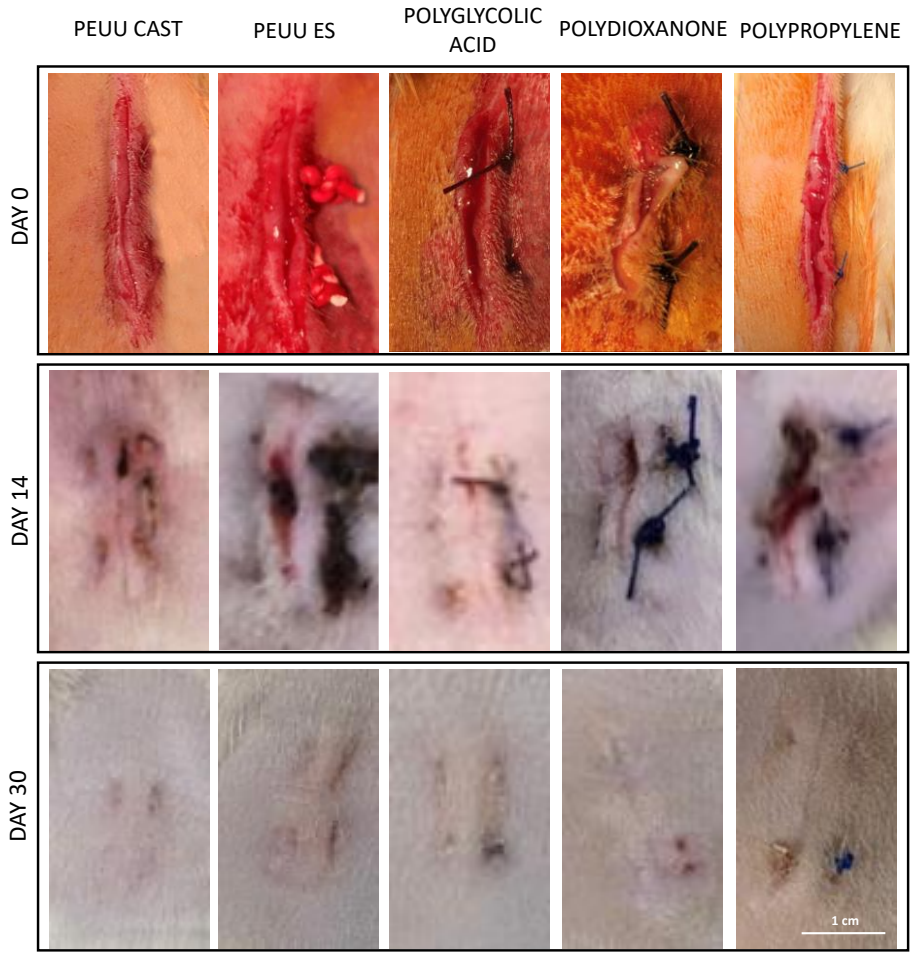

Figure 21 Visual inspection of suture healing at day 0, day 14 and day 30 after the sacrifice.

Histological sections were imaged at 5x magnification using a Zeus live-cell microscope. The histological visual inspection of the explants showed significant differences between groups in terms of

cellular infiltration, adipose tissue and collagen deposition and hair follicle (**Figure 22**A). The explant visual inspection was coupled with quantitative measurements. Images were cut among the area of interest and collagen density under the wound was evaluated and compared to the rat healthy skin. Despite the gross observation showed complete epithelialization at day 30, quantitative analysis results evaluated that collagen density was less in the PGA and PDS group when compared to the healthy skin group ($p < 0.05$) (**Figure 22**B).

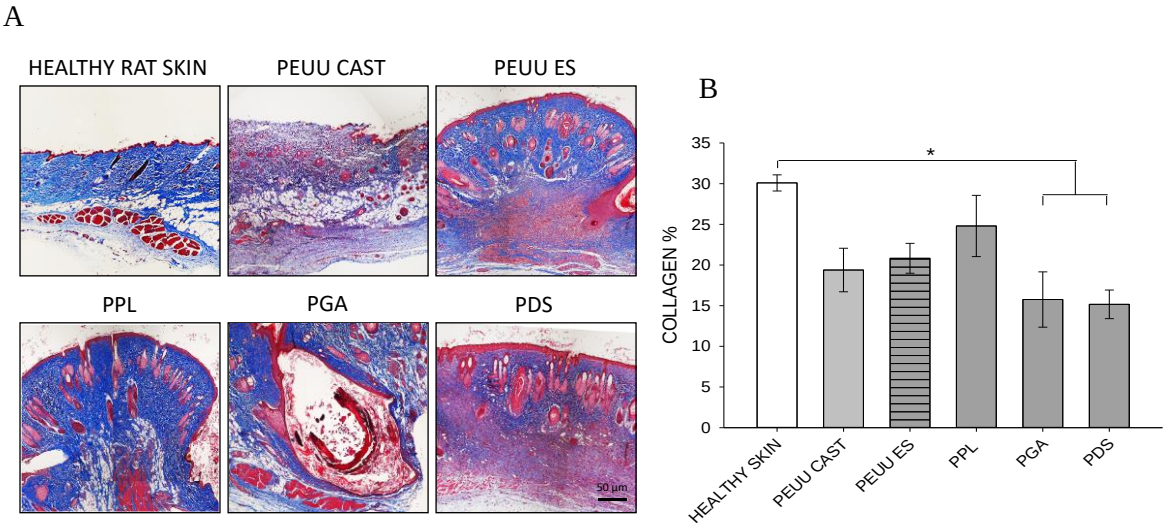

Figure 22 Collagen remodeling. *A) Qualitative histological evaluation. Masson's Trichrome staining was used to evaluate the ex-novo tissue, cellular infiltration and scar formation of 30-days explants compared to healthy rat tissue. B) Collagen quantitative analysis. The suture body response was analyzed using the method of D'Amore, A. et al. 2018[17] which utilizes a custom image analysis algorithm developed with MatLab (The MathWorks, Natick, MA). Average collagen percentage under the 30-days sutured area compared to normal skin collagen percentage. One Way ANOVA shows statistically significant differences among the groups. * = $p < 0.05$.*

Ex vivo inflammatory host response assessment

The spatial distribution of phenotypically distinct macrophages at the wound section was characterized by immunolabeling. The co-expression of the pan-macrophage cell-surface marker CD11b with the M1-like pro-inflammatory marker iNOS and/or M2-like anti-inflammatory marker Fizz1 was determined (**Figure 23**A). After 30 days all suture materials induced a macrophage response. The population of anti-inflammatory (M2-like) macrophages, recognized as Fizz1+ cells, showed significant differences between groups. M2-like phenotype macrophages were in higher number in the PEUU ES and in the PGA groups. Statistical analysis of M2-like macrophage population showed differences ($p < 0.05$) between PGA vs. Healthy, PDS and PEUU Cast and between PEUU ES vs. Healthy, PDS and PEUU

Cast, as indicated **Figure 23**C (Fizz bar chart). Quantification of pro-inflammatory (M1-like) macrophages, recognized ad iNOS+ cells, showed a greatest number of cells in PPL, PGA and PDS groups. Statistical analysis did not show any differences for this subpopulation of macrophages between the groups (**Figure 23**C, iNOS bar chart). Differences observed in M2 and M1 macrophage subpopulations among the groups were reflected in the ratio of M2-like:M1-like macrophages. The M2-like:M1-like ratio showed a different response for each group implanted. The ratio was higher for PEUU ES than for the other groups (**Figure 23**B).

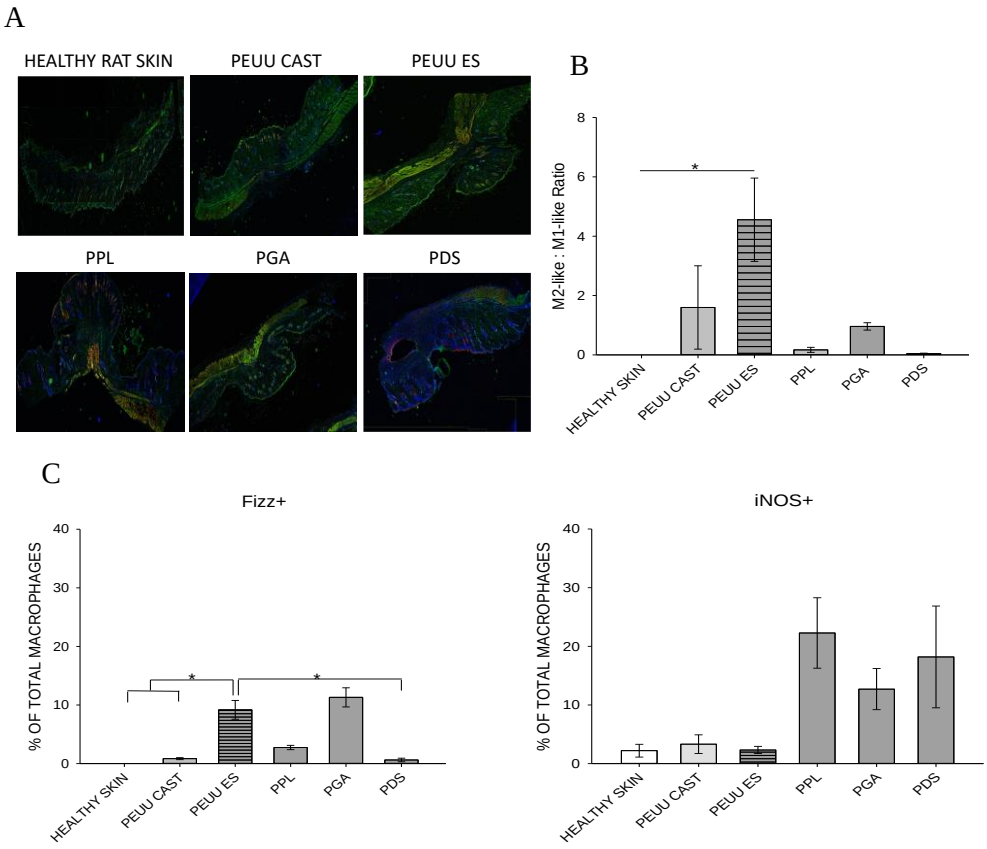

Figure 23 Inflammatory host response evaluation. *A) Qualitative immunohistochemical evaluation. Immunohistochemistry was used to evaluate macrophage phenotype of 30-days explants compared to healthy rat tissue. B) Quantification of M2-like:M1-like ratio of macrophages. Ratio of M2-like:M1-like in the sutured area. Images were quantified using CellProfiler image analysis software. In vivo, PEUU ES suture wire modulates an anti-inflammatory macrophage phenotype. Differences between groups were evaluated using ANOVA test. * = $p < 0.05$. C) Immunoblotting quantitative results. Bar charts show the densitometry quantification of pro- and anti-inflammatory protein expression iNOS and Fizz. One Way ANOVA test showed statistically significant differences between means. * = $p < 0.05$.*

Evaluation of pre- and post-implant suture wires uniaxial mechanical properties

Figure 24 shows the uniaxial mechanical properties of the suture wires used for the study in vivo before and after implantation. After 30 days, rats were sacrificed and suture wires, where present, were collected for the mechanical evaluations. The uniaxial tensile test was performed on a horizontal MTS TytronTM 250 machine following the *D2256/D2256M Standard test method for tensile properties of yarns by the single-strand method*. Samples were subjected to 0.75 N preload and strained at a speed of 25 mm/min until failure to determine the complete stress/strain curve. The initial modulus bar chart shows the initial modulus, measured in megapascal, of pre- and post-implant suture wires. The pre-implant suture initial modulus was compared to the rat skin initial modulus. Results of Brown-Forsythe and Welch ANOVA showed statistically significant differences between the pre-implant PEUU Cast, PPL, PGA and PDS groups versus the rat skin control group. Statistical analysis showed no significant difference between PEUU ES and rat skin groups. The strain at break bar chart shows the strain at break, in percentage, of pre- and post-implant suture wires. Results of Brown-Forsythe and Welch ANOVA showed statistically significant differences between the pre implant PEUU Cast and PEUU ES groups versus the rat skin control group. The ultimate tensile strength bar chart shows the ultimate tensile strength, measured in megapascal, of pre- and post-implant suture wires. Results of Brown-Forsythe and Welch ANOVA shown statistically significant differences between the pre implant PPL, PGA and PDS groups versus the rat skin control group. The analysis showed no significant difference between PEUU Cast and ES and rat skin groups.

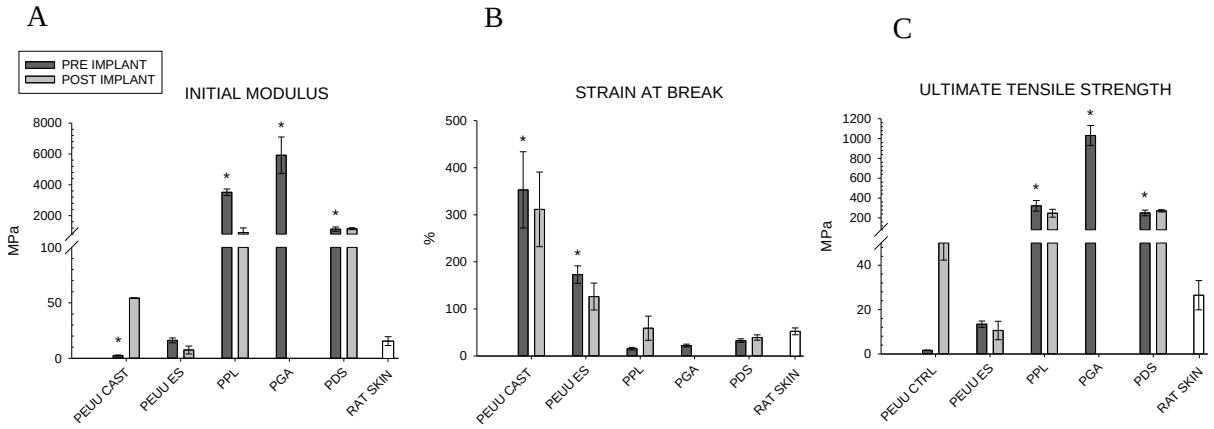

Figure 24 Suture wire pre- and post-implant mechanical properties. *After 30 days the rats were sacrificed and the suture wires, where present, were collected for the mechanical evaluations. The uniaxial tensile test was performed on a horizontal MTS TytronTM 250 machine. Samples were subjected to 0.75 N preload and strained*

*at a speed of 25 mm/min until failure to determine the complete stress/strain curve. A) Initial modulus. The bar chart shows the initial modulus, measured in megapascal, of pre- and post-implant suture wires. The pre-implant suture initial modulus was compared to the rat skin initial modulus. Results of Brown-Forsythe and Welch ANOVA shown statistically significant differences between the pre implant PEUU Cast, PPL, PGA and PDS groups versus the rat skin control group. Analysis showed no significant difference between PEUU ES and rat skin groups. * = $p < 0.05$. B) Strain at break. The bar chart shows the strain at break, in percentage, of pre- and post-implant suture wires. Results of Brown-Forsythe and Welch ANOVA shown statistically significant differences between the pre implant PEUU Cast and PEUU ES groups versus the rat skin control group. * = $p < 0.05$. C) Ultimate tensile strength. The bar chart shows the ultimate tensile strength, measured in megapascal, of pre- and post-implant suture wires. Results of Brown-Forsythe and Welch ANOVA shown statistically significant differences between the pre implant PPL, PGA and PDS groups versus the rat skin control group. Analysis showed no significant difference between PEUU Cast and ES and rat skin groups. * = $p < 0.05$.*

Biaxial mechanical characterization of rat skin

Equi-membrane tension biaxial testing (**Figure 25**) was performed to characterize the mechanics of explanted tissue in the region of the sutured area 30 days after surgery. All groups showed an increase in stiffness over the longitudinal direction when compared to the circumferential direction. There were no statistically significant differences between the groups and the healthy rat skin control group.

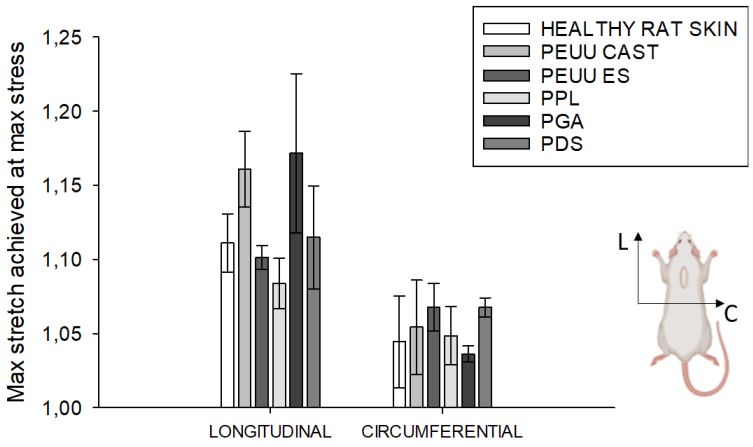

Figure 25 Rat skin pre- and post-implant biaxial properties. *After 30 days the rats were sacrificed and the back skins were collected for the mechanical evaluations. The biaxial test was performed on a custom-build planar biaxial stretching system. Sutured rat skins were compared to healthy rat skin. Sample mechanical characterization showed no differences among groups.*

BIOMECHANICAL ASSESSMENT OF BIOMIMETIC ENGINEERED CHORDAE TENDINEAE

Scanning electron microscopy and study of fiber deposition

Native porcine CT, BECT and microintegrated BECT surface characterization and quantitative analysis of fiber deposition have been conducted. Seven randomly chosen images were selected for each of the three sample groups. Image analysis of dry and microintegrated BECTs revealed highly aligned microscopic fibers that duplicate native tissue anatomy (**Figure 26**). The inclusion of cell culture into the construct induced a distinct change in scaffold microarchitecture. Quantitative structure information were obtained by the use of a custom made MatLab algorithm[22]. Despite the structural differences between groups, fiber diameter remained consistent among the analyzed groups. Differences in fabrication technique were reflected in the fiber orientation. Statistical analysis showed differences ($p < 0.05$) between dry and microintegrated BECTs (**Figure 27**).

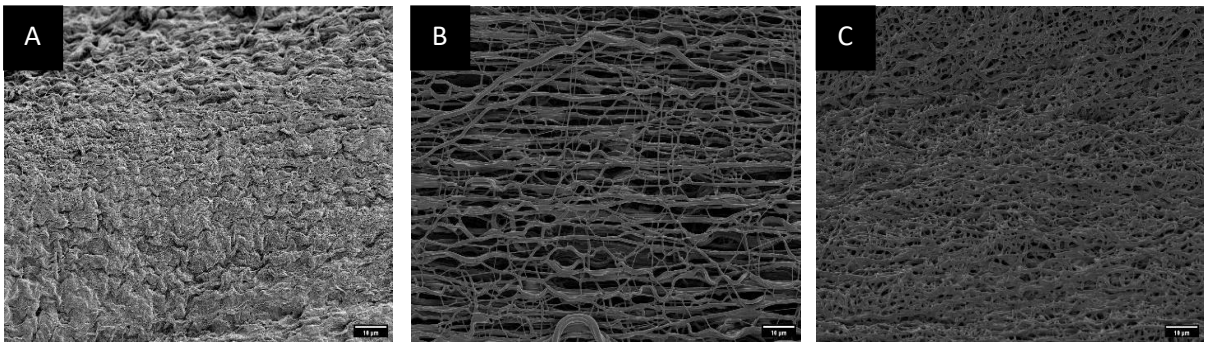

Figure 26 Scanning electron microscopy of native CT and BECTs. *SEM analysis at 1000X magnification (scale bar 10 microns). 7 images per group were randomly collected to characterize the CT and BECT ultrastructure. A) Native porcine CT. B) Dry BECT. C) Microintegrated BECT.*

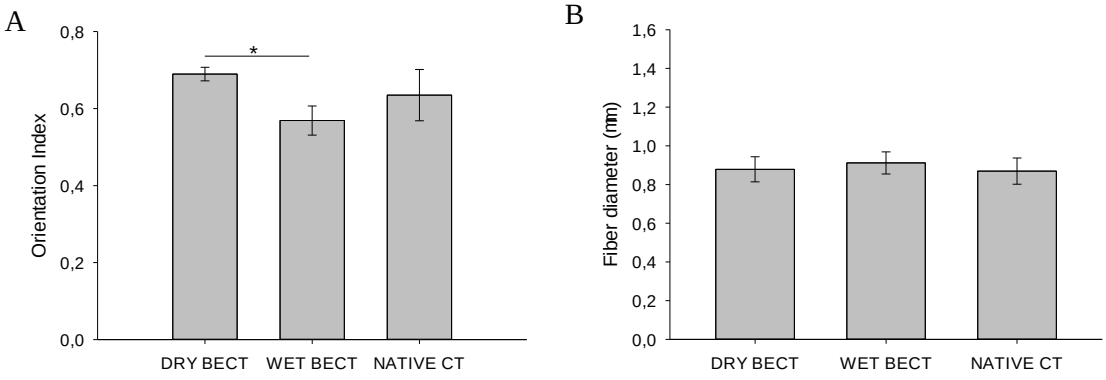

Figure 27 Native CT and BECT fiber analysis. *Orientation Index and Fiber diameter were characterized using the method of D'Amore, A. et al. 2010[22]. A) Orientation Index characterization showed no differences in fiber*

*orientation between BECT and native CT, statistical differences are showed between dry and wet BECT. * = $p < 0.05$ B) Fiber diameter remain consistent among the groups.*

Hematoxylin and Eosin

Histological analysis was carried out on BECT samples, with and without microintegrated cells, at 24 hours and after 3 days of static culture plus seven days of treatment. H&E staining was used for generical morphological assessment. Scaffolds were imaged at 20x magnification using a Zeus live-cell microscope. Visual inspection of the explants showed significant differences between groups in terms of cellular infiltration and scaffold remodeling. H&E staining showed that 24 hours after micro-integration only a few cells were inside the scaffold. Moreover, the inclusion of cells into the BECTs resulted in a dramatic change in scaffold fiber bonding and microarchitecture compared to the scaffold without cells. However, after three days of static culture plus seven days of different conditioning, the cells have grown dense and tightly connected in all BECT scaffolds groups. As for comparative evaluation of BECT groups: the static in plate group showed less cellular infiltration and lower scaffold remodeling, the static in tension group showed higher fiber bonding and cell infiltration. Compared to the other groups, the dynamic group showed higher cellular infiltration, with cells better organized, densely and tightly connected, and higher scaffold remodeling. In **Figure 28** representative H&R-stained histological cross sections of BECTs.

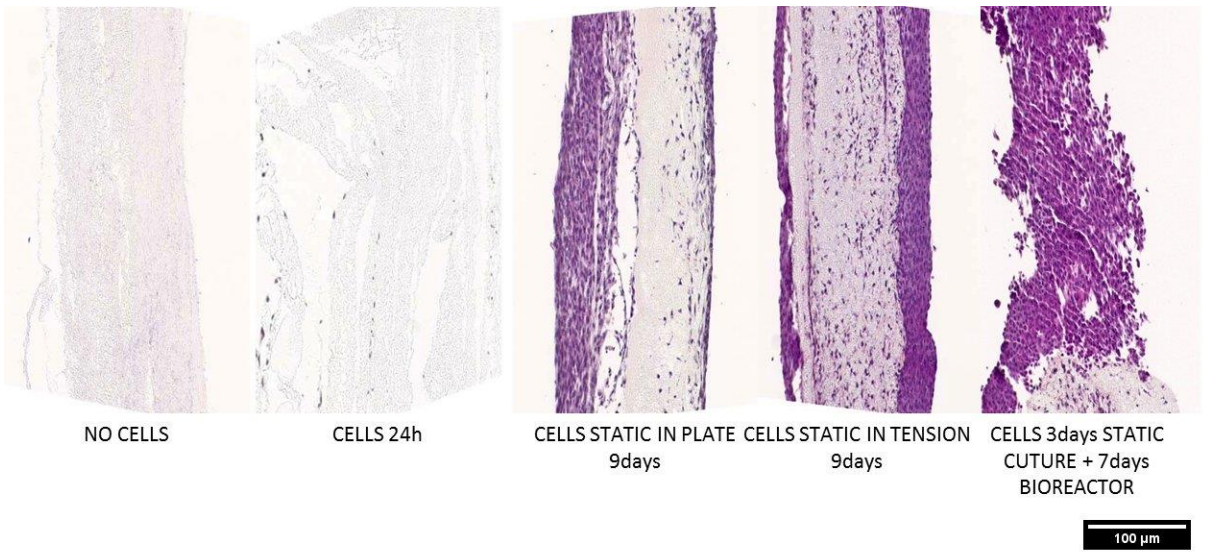

Figure 28 Histological evaluation of microintegrated BECTs. *Qualitative histological evaluation. Hematoxylin and Eosin staining was used to evaluate cellular infiltration and scaffold remodeling.*

Uniaxial mechanical characterization of BECTs

Figure 29 shows the uniaxial mechanical properties of the BECTs, with and without cells, after the conditioning period. The initial modulus bar chart shows the initial modulus measured in megapascal. The ANOVA results showed that the initial modulus was significative greater in the BECTs without cells and in the dynamic group compared to the groups in tension and in plate. The strain at break bar chart shows the strain at break in percentage. The ANOVA results did not show any statistical differences between groups. The ultimate tensile strength bar chart shows the ultimate tensile strength measured in megapascal. The ANOVA results showed that the ultimate tensile strength was significative greater in the BECTs without cells compared to the group in tension and in plate. After one week the BECTs exposed at 30% of strain cyclic elongation in the dynamic group showed a statistically higher initial modulus and higher ultimate tensile strength compared to the static in plate and static in tension groups. There is no statistical difference between the no cell group and the dynamic group.

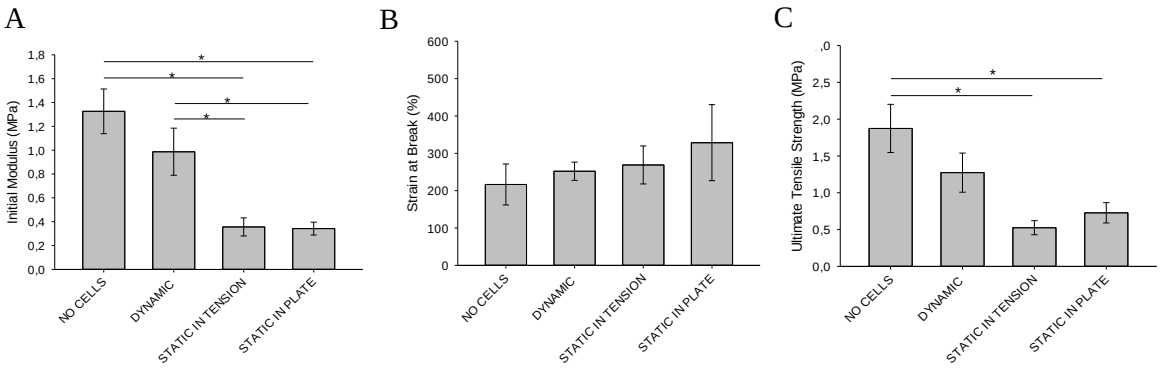

Figure 29 BECT uniaxial tensile test. *After conditioning BECTs were collected for the mechanical evaluations. The uniaxial tensile test was performed on a horizontal MTS TytronTM 250 machine. Samples were strained at a speed of 1 mm/min until failure to determine the complete stress/strain curve. A) Initial modulus. The bar chart shows the BECT initial modulus, measured in megapascal ANOVA results showed statistically significant differences between No Cell and Dynamic groups versus Static in plate and Static in tension groups.* ***** *= $p < 0.05$. B) Strain at break. The bar chart shows the strain at break, in percentage. Analysis showed no significant difference among groups. C) Ultimate tensile strength. The bar chart shows the ultimate tensile strength, measured in megapascal. Results of ANOVA test showed statistically significant differences between the No Cell group versus the Static in plate and Statin in tension groups* ***** *= $p < 0.05$.*

DISCUSSION

It was amply demonstrated that electrospun scaffold structure induces biological cell activity, proliferation and differentiation[41]. Several authors have discussed the importance of fabricating electrospun filaments and yarns because they will have a huge potential in tissue engineering and may be employed in soft tissue injury treatment. In particular, they can be used to create biocompatible scaffolds and medical sutures with tailored mechanical and structural properties. For instance, electrospun wires can be applied for tendon and ligament replacement in orthopedic surgery or CT replacement in cardiac surgery. For the aforementioned reasons, due to their intrinsic structure, electrospun wires will provide a favorable mechanical and structural environment able to mimic the hierarchical ECM structure and the mechanical properties of the native tissue. However, despite the electrospun wire potential, only a limited fraction of studies has stressed the development of this technology. So far, electrospun wires have been created using a wide range of collectors: liquid surfaces[38, 58, 63, 69], static funnels[2, 4, 35, 44], disks[5], moving targets as cylinders or rollers[34, 48, 67], actual wires[49] or, some authors, changed the electrospinning set up[23]. Nevertheless, these techniques demonstrated limits in control and reproducibility and the filaments obtained exhibited some limits in their structure and mechanical properties. Moreover, just in a few of these studies, safety and electrospun wires in vitro and in vivo performances have been evaluated.

In this study, a novel mandrel-less electrodeposition methodology to create polymeric microfiber wire was introduced. The polymeric fibers are collected between two facing electrodes that macroscopically span from an electrode to the other inducing a deposition-aligned microfiber. Two versions of this method are presented.

A static version (**Figure 12**), that consists in two faced electrodes that allow the high aligned deposition of electrospun microfibers. This electrode set was used to fabricate PCUU BECTs with 2 cm length spanning.

A dynamic version (**Figure 6**), used to fabricate PEUU suture wires with virtually no limitation in longitudinal length. The electrospun suture wire apparatus, used for electrospun suture wire fabrication, consists in two towers containing a rotating spindle, chucks for mandrels, and drive motors. Both towers allow start/stop and variable speed rotation of the device's main central axis. One of the towers contains a take-up spool for the spool collection. Clutch torque, take-up speed, and take-up direction can be controlled.

The first part of this study was focused on the electrospun suture wire *in vitro* and *in vivo* assessment. First, a finite element analysis of the suture apparatus electric field was conducted and a 2D and 3D models were created using COMSOL Multiphysics (**Figure 15**). As experimentally observed the lines of the electrical field departed from the spinneret to the electrodes, corroborated the hypothesis that

between the facing electrodes the electric charges increase dramatically. As mentioned, the device used to obtain the suture wire was equipped with two motors, different types of microfiber deposition were obtained by changing the mandrel rotation. Using SEM analysis, the possibility to modify the wire micro-architecture and mechanical properties was evaluated and proved (**Figure 16**). The wire surfaces were analyzed using a custom made MatLab algorithm (**Figure 17**). The registered fiber orientation showed consistency with the known fiber alignment-electrode rotation relationship (**Figure 17**A) and the orientation angle changes as well based on the electrode rotation used (**Figure 17**B). However, fiber diameter, pore size and porosity remained consistent among the groups. Macroscopically, the cross-section diameter versus deposition time was evaluated and results showed that, at constant fabrication variables, the wire diameter increases among the time (**Figure 18**A). In order to better understand how different micro-architectures can affect the wire mechanical properties uniaxial tensile test was performed. A total of six different configurations were tested: a PEUU Cast wire as control and five different electrospun configurations (fabrication variables are showed in **Table 1**). As the initial modulus bar chart showed, (**Figure 18**B) changes in fiber arrangement resulted in modifying the uniaxial mechanical properties of the electrospun suture wires while delivering the identical polymer mass during the deposition process, which enables them to be tailored for a multitude of applications. Macrophage response is a critical determinant of the host response. The present study showed a macrophage phenotype response to PEUU ES suture wire *in vitro* and *in vivo*. PEUU Cast and ES degradation products have been evaluated *in vitro*, at two different concentrations, by IHC, 1:10 and 1:50, on a BMM cell population. Exposure of BMM to PEUU ES degradation product 1:50 showed a decrease in the number of M1-like cells compared to the other treatments. The PEUU ES degradation products 1:10 increased the percentage of M2-like cells when compared to the PEUU ES degradation products 1:50. PEUU Cast degradation products 1:50 showed a decrease in the number of M2-like macrophages compared to the other treatments (**Figure 19**). Results showed the PEUU ES degradation product elicits a more robust anti-inflammatory response. The cause for the more pronounced M2-like reaction to the PEUU ES degradation compared to the M1-like reaction to the PEUU Cast is unknown. This result can be related to different degradation rates.

In order to better understand if the macrophage phenotype was also stimulated by the texture of the scaffold, BMM were seeded onto a PEUU ES and Cast 2D scaffold configurations and the Arginase1 and iNOS expressions were evaluated by immunoblotting. According to the results obtained with the degradation products, macrophages seeded on the PEUU ES showed an increase in the expression of Arginase 1, M2-like phenotype marker, when compared to the PEUU Cast (**Figure 20**B). Then, macrophage phenotype was evaluated, by IHC, when seeded onto electrospun suture wires. Significant changes were observed on macrophage phenotype when seeded onto a 3D electrospun wire PEUU scaffold. Macrophages showed an increase of Fizz expression when compared to iNOS (**Figure 20**D). Results suggested PEUU ES scaffolds, both flat 2D surface or 3D wire, evocate a M2-like anti-inflammatory reaction in seeded macrophages. Finally, the PEUU ES suture wire was evaluated in vivo

in a rat model. PEUU ES performances were compared to some of the most common suture materials: PPL, PGA and PDS. Thirty days after surgery, the surgical wound visual evaluation did not show any macroscopical difference (**Figure 21**). However, during the explant histological inspection, significant differences between groups in terms of cellular infiltration, adipose tissue and collagen deposition have been founded. Despite the gross observation showed complete epithelialization, collagen deposition quantitative analysis showed that collagen was less deposited in the PGA and PDS group when compared to the healthy skin group (**Figure 22**B). The analysis did not show any statistically significant differences between PEUU ES and PEUU Cast versus the healthy skin control group. In vivo inflammation was evaluated using IHC analysis. Results showed statistical differences among groups. The number of M2-like anti-inflammatory macrophages was higher in the PEUU ES and in the PGA groups (**Figure 23**C). Differences observed in the subpopulation of macrophages for each used suture materials were reflected in the M2-like:M1-like ratio (**Figure 23**B). The analysis showed a differential response among materials with a higher M2-like:M1-like ratio for PEUU ES group. The *in vivo* results suggested that PEUU ES wires improved collagen deposition (**Figure 22**) and reduced macrophage pro-inflammatory response promoting the M2-like macrophage phenotype (**Figure 23**).
Uniaxial tensile test was conducted on suture wires before and after the *in vivo* use (**Figure 24**). PGA sutures were completely biodegraded after 30 days in contrast to PDS suture that entirely preserved the mechanical properties. Almost all of the groups showed significant differences versus the rat skin control group. However, PEUU ES did not show any statistical difference versus the rat skin and its mechanical properties were still preserved after the *in vivo* test. Moreover, biaxial test was conducted in order to test the scar tissue mechanical properties (**Figure 25**). The ANOVA test did not show any difference between the explants and the healthy rat skin, confirming the histological evaluation that did not show any fibrotic tissue among the groups.

There are several limitations to the present study. Limited markers were used to determine the macrophage phenotype among the *in vitro* and *in vivo* experiments. Due to the physical limitation of the *in vitro* macrophage seeding on the suture wire, the immunohistochemical evaluation was preferred instead of the immunoblotting. However, previous results on 2D scaffolds were conducted using immunoblotting, due to the difficulty in the image acquisition through the material. Another limitation is that the study only evaluates a single time point and a single sutured area. In addition, the suture material chosen for this study represents a small set of degradable and not degradable suture material present on the market.

The second part of this work was focused on the BECTs in vitro assessment. Preliminary results on microintegrated high aligned PCUU fiber scaffold produced by mandrel-less electrospinning were presented. SEM analysis was applied to characterize the native porcine CT, dry PCUU BECT and microintegrated BECT surfaces (**Figure 26**). Image analysis of dry and microintegrated BECTs revealed highly aligned microscopic fibers that duplicate native tissue anatomy. The registered BECT fiber

orientation showed consistency with the supposed fiber alignment. However, the inclusion of cells during the fabrication drastically changed the scaffold microarchitecture. Native CT and bioengineered construct surfaces were analyzed using a custom made MatLab algorithm (**Figure 27**). Despite the structural differences, fiber diameter remained consistent among the groups. Microintegrated BECTs were divided in groups, static in plate, static in tension and dynamic. After 7 days the histological results and the mechanical properties were evaluated. H&E histological analysis showed significant changes between groups. At the end of the conditioning, the static in plate group exhibited less fibroblast infiltration and lower scaffold remodeling compared to the other groups. Stating in tension group showed higher fiber bonding and cell infiltration from the scaffold surfaces. The dynamic group revealed significative scaffold remodeling with fibroblasts densely and tightly connected (**Figure 28**). In order to better understand if the in vitro scaffold remodeling affected the mechanical behavior, we investigate how mechanical conditioning of microintegrated high aligned scaffolds affected the mechanical properties. The uniaxial mechanical properties of BECTs showed that mechanical properties improved in the dynamic group. Compared to the static controls, initial modulus of BECTs conditioned in the bioreactor was significantly higher (**Figure 29**). The improvements in mechanical properties with bioreactor conditioning are in line with previous evidences[59, 68].

However, several limitations will be addressed during future work for better understanding how the mechanical and biochemical stimuli influence proliferation and cell phenotype. First, this study only evaluates a single time point. Multiple time points, up to 30 days of conditioning, will be tested. Second, only one histological staining was evaluated. Masson's Trichrome, Picrosirius red and confocal measurements will be performed to evaluate cell proliferation and *ex novo* tissue formation. Biochemical analysis will be carried out in order to evaluate *ex novo* collagen, elastin and glycosaminoglycan and cellular genetical expression will be assessed.

CONCLUSIONS

Fibrillar structures are widely represented in nature. Is well established that electrospun microfibers can mimic the native ECM fibrils in terms of scale and spatial disposition. It was amply demonstrated that bioengineered electrospun microfiber scaffolds induce biological cell activity and provide several advantages in terms of cell infiltration and ex novo tissue formation. However, despite the research progress made in the tissue engineering field, the inability to accurately deposit fibers are still a major drawback in the advances of electrospinning. Due to these technical limitations, little effort has been made to develop a stable methodology for electrospun filament fabrication. A new electrospinning apparatus and a mandrel-less electrode set were introduced. Mandrel-less electrospinning deposition allows the fabrication of wire with axial symmetry and virtually no limitation in longitudinal length. The findings of this study offer a promising and versatile processing methodology with the capacity to control the structure, function and mechanical properties of electrospun wires. The data presented in this work are strictly related to the tissue engineering application, like tendon and ligament replacement and medical fiber uses. Though, the use of electrospun wires with tunable properties can be extended for a larger variety of applications.

Acknowledgments

First and foremost, I would like to express my sincere appreciation and gratitude to my advisor, Prof. Antonio D'Amore, for his guidance, mentorship, help and support during these years. Although I had no previous experience in tissue engineering, Antonio helped me to understand and encourage me to think and explore independently, yet he was always by my side to advise whenever I needed.
I consider Antonio not only my mentor, but my friend too.

I would also like to thank my co-advisor Prof. Giulio Ghersi and my PhD program coordinator Prof. Maurizio Leone, thanks to everything you helped me to accomplish.

Thank you to all those that helped me and made my work interesting, fun and exciting!

Thanks to all of my colleagues from the University of Palermo: Laura, Giorgia, Simona, Silvia, Monica. I learned a lot from them during my time in Palermo, personally as well as professionally.

I would like to thank all of the professors and colleagues from the McGowan Institute for Regenerative Medicine at the University of Pittsburgh. Thanks to Dr. Wagner and Dr. Badylak, Sam, Amrita, Andreas, Maria Giovanna, Sunita, Janani, Arthi, Salma, Bill, David, Joe, Mangesh, Bane, Drake, Sruthi, Shiv, Tommaso, Neil, Scott, Lina, Catalina, Seungil and many others for all the advices, help and food. Thanks to the Machining Shop and in particular to Dan Mckeel, one of the best men that I met in my life. Thanks to the CBI staff, especially Jonathan Franks, that helped me with the SEM and keep me company while I was using the microscope. It has been a pleasure working with all of them.

I would also like to thank all of the students from the D'Amore Laboratory for support, help and friendship. Thanks to Marco, Gianluca, Francesco, Haider, Mahdi and Anna.

A special mention goes to my friends.

Thanks to Giorgio and Ruby, my freaky Pitt-family, I am so happy I met them. They have always been there for me: we have laughed, worked, cooked and planned together, we shared our ideas, dreams and fears. I really miss them in my daily life.

Thanks to Pietro and Federica, friends and now lab mates, for making the work always fun and interesting, for all the help and the incredible ideas and advice. I am really glad that we can work together and learn more and more.

I do not have words to describe the surprise to find real friends during this season of my life.

Thank you to Carlo, I am so blessed to have him in my life. He is a strong man, symbol of resilience and determination for me. His continuous support and guidance helped me when I had been feeling weak and confused. I cannot imagine be away from you again.

Finally, I would like to thank my family. My mother Elisa and my father Elio, who always remember me that I am strong and independent. My brother Gabriele, who always finds the bright side and makes funny faces and stupid jokes just to see how I react. Thank you to all of your support, your trust and kindness. All of this would not have been possible without you!

Bibliography

1. The Heart. In: *Quain's Anatomy*, edited by e. Walmsley T. London: Longman, Green and Co., 1929, pp. 81.

2. Afifi A. M., S. Nakano, H. Yamane and Y. Kimura. Electrospinning of continuous aligning yarns with a 'funnel'target. *Macromolecular Materials and Engineering* 295: 660-665, 2010.

3. Ahmed F., I. A. Shaikh, T. Hussain, I. Ahmad, S. Munir and M. Zameer. Developments in health care and medical textiles-A mini review-1. *Pakistan Journal of Nutrition* 13: 780, 2014.

4. Ali U., Y. Zhou, X. Wang and T. Lin. Direct electrospinning of highly twisted, continuous nanofiber yarns. *Journal of the Textile Institute* 103: 80-88, 2012.

5. Bazbouz M. B. and G. K. Stylios. Novel mechanism for spinning continuous twisted composite nanofiber yarns. *European polymer journal* 44: 1-12, 2008.

6. Bhardwaj N. and S. C. Kundu. Electrospinning: a fascinating fiber fabrication technique. *Biotechnology advances* 28: 325-347, 2010.

7. Bosworth L., N. Alam, J. Wong and S. Downes. Investigation of 2D and 3D electrospun scaffolds intended for tendon repair. *Journal of Materials Science: Materials in Medicine* 24: 1605-1614, 2013.

8. Brown B. N., B. D. Ratner, S. B. Goodman, S. Amar and S. F. Badylak. Macrophage polarization: an opportunity for improved outcomes in biomaterials and regenerative medicine. *Biomaterials* 33: 3792-3802, 2012.

9. Butany J., M. J. Collins and T. E. David. Ruptured synthetic expanded polytetrafluoroethylene chordae tendinae. *Cardiovascular pathology* 13: 182-184, 2004.

10. Caimmi P. P., M. Sabbatini, L. Fusaro, A. Borrone and M. Cannas. A study of the mechanical properties of ePTFE suture used as artificial mitral chordae. *Journal of cardiac surgery* 31: 498-502, 2016.

11. Caimmi P. P., M. Sabbatini, L. Fusaro and M. Cannas. Politetrafluorene suture used as artificial mitral chord: mechanical properties and surgical implications. *The Journal of cardiovascular surgery* 58: 895-903, 2017.

12. Capulli A., L. MacQueen, S. P. Sheehy and K. Parker. Fibrous scaffolds for building hearts and heart parts. *Advanced drug delivery reviews* 96: 83-102, 2016.

13. Chang H., M. Hu, H. Zhang, K.-f. Ren, B.-c. Li, H. Li, L.-m. Wang, W.-x. Lei and J. Ji. Improved endothelial function of endothelial cell monolayer on the soft polyelectrolyte multilayer film with matrix-bound vascular endothelial growth factor. *ACS applied materials & interfaces* 8: 14357-14366, 2016.

14. Chen S., A. N. Annaidh and S. Roccabianca. A microstructurally inspired constitutive model for skin mechanics. *Biomechanics and Modeling in Mechanobiology* 19: 275-289, 2020.

15. Courtney T., M. S. Sacks, J. Stankus, J. Guan and W. R. Wagner. Design and analysis of tissue engineering scaffolds that mimic soft tissue mechanical anisotropy. *Biomaterials* 27: 3631-3638, 2006.

16. Coutinho G. F., L. Carvalho and M. J. Antunes. Acute mitral regurgitation due to ruptured ePTFE neo-chordae. 2007.

17. D'Amore A., M. Fazzari, H.-B. Jiang, S. K. Luketich, M. E. Luketich, R. Hoff, D. L. Jacobs, X. Gu, S. F. Badylak and B. A. Freeman. Nitro-oleic acid (NO2-OA) release enhances regional angiogenesis in a rat abdominal wall defect model. *Tissue Engineering Part A* 24: 889-904, 2018.

18. D'Amore A., S. K. Luketich, G. M. Raffa, S. Olia, G. Menallo, A. Mazzola, F. D'Accardi, T. Grunberg, X. Gu and M. Pilato. Heart valve scaffold fabrication: Bioinspired control of macro-scale morphology, mechanics and micro-structure. *Biomaterials* 150: 25-37, 2018.

19. D'Amore A., J. S. Soares, J. A. Stella, W. Zhang, N. J. Amoroso, J. E. Mayer Jr, W. R. Wagner and M. S. Sacks. Large strain stimulation promotes extracellular matrix production and stiffness in an elastomeric scaffold model. *Journal of the mechanical behavior of biomedical materials* 62: 619-635, 2016.

20. D'amore A. and W. R. Wagner. Mandrel-Less Electrospinning Processing Method and System, and Uses Therefor. Google Patents, 2020.

21. D'Amore A., T. Yoshizumi, S. K. Luketich, M. T. Wolf, X. Gu, M. Cammarata, R. Hoff, S. F. Badylak and W. R. Wagner. Bi-layered polyurethane–extracellular matrix cardiac patch improves ischemic ventricular wall remodeling in a rat model. *Biomaterials* 107: 1-14, 2016.

22. D'Amore A., J. A. Stella, W. R. Wagner and M. S. Sacks. Characterization of the complete fiber network topology of planar fibrous tissues and scaffolds. *Biomaterials* 31: 5345-5354, 2010.

23. Dabirian F., Y. Hosseini and S. H. Ravandi. Manipulation of the electric field of electrospinning system to produce polyacrylonitrile nanofiber yarn. *Journal of the Textile Institute* 98: 237-241, 2007.

24. Dart A. and C. Dart. Suture Material: Conventional and Stimuli Responsive. 2017.

25. David T. E. Artificial chordae. In: *Seminars in thoracic and cardiovascular surgery*Elsevier, 2004, p. 161-168.

26. Doshi J. and D. H. Reneker. Electrospinning process and applications of electrospun fibers. *Journal of electrostatics* 35: 151-160, 1995.

27. Englen M., Y. Valdez, N. Lehnert and B. Lehnert. Granulocyte/macrophage colony-stimulating factor is expressed and secreted in cultures of murine L929 cells. *Journal of immunological methods* 2: 281-283, 1995.

28. Enoch S. and D. J. Leaper. Basic science of wound healing. *Surgery (Oxford)* 26: 31-37, 2008.

29. Fan R., A. S. Bayoumi, P. Chen, C. M. Hobson, W. R. Wagner, J. E. Mayer Jr and M. S. Sacks. Optimal elastomeric scaffold leaflet shape for pulmonary heart valve leaflet replacement. *Journal of biomechanics* 46: 662-669, 2013.

30. Fishman J. M., K. Wiles and K. J. Wood. The acquired immune system response to biomaterials, including both naturally occurring and synthetic biomaterials. In: *Host Response to Biomaterials*Elsevier, 2015, pp. 151-187.

31. Gordon S. Taylor PR. *Monocyte and macrophage heterogeneity. Nat Rev Immunol* 5: 953-964, 2005.

32. Guan J., M. S. Sacks, E. J. Beckman and W. R. Wagner. Biodegradable poly (ether ester urethane) urea elastomers based on poly (ether ester) triblock copolymers and putrescine: synthesis, characterization and cytocompatibility. *Biomaterials* 25: 85-96, 2004.

33. Gunnal S., R. Wabale and M. Farooqui. Morphological study of chordae tendinae in human cadaveric hearts. *Heart views: the official journal of the Gulf Heart Association* 16: 1, 2015.

34. Hajiani F., A. A. Jeddi and A. Gharehaghaji. An investigation on the effects of twist on geometry of the electrospinning triangle and polyamide 66 nanofiber yarn strength. *Fibers and Polymers* 13: 244-252, 2012.

35. He J., Y. Zhou, K. Qi, L. Wang, P. Li and S. Cui. Continuous twisted nanofiber yarns fabricated by double conjugate electrospinning. *Fibers and Polymers* 14: 1857-1863, 2013.

36. Hong Y., J. Guan, K. L. Fujimoto, R. Hashizume, A. L. Pelinescu and W. R. Wagner. Tailoring the degradation kinetics of poly (ester carbonate urethane) urea thermoplastic elastomers for tissue engineering scaffolds. *Biomaterials* 31: 4249-4258, 2010.

37. Jones K. Fibrotic response to biomaterials and all associated sequence of fibrosis. In: *Host response to biomaterials*Elsevier, 2015, pp. 189-237.

38. Khil M. S., S. R. Bhattarai, H. Y. Kim, S. Z. Kim and K. H. Lee. Novel fabricated matrix via electrospinning for tissue engineering. *Journal of Biomedical Materials Research Part B: Applied Biomaterials: An Official Journal of The Society for Biomaterials, The Japanese Society for Biomaterials, and The Australian Society for Biomaterials and the Korean Society for Biomaterials* 72: 117-124, 2005.

39. Kümmerle J. M. and C. Fogle. Suture materials and patterns. *Equine Surgery-E-Book* 43: 255, 2018.

40. Kyriakides T. R. Molecular Events at Tissue–Biomaterial Interface. In: *Host Response to Biomaterials*Elsevier, 2015, pp. 81-116.

41. Li W. J., C. T. Laurencin, E. J. Caterson, R. S. Tuan and F. K. Ko. Electrospun nanofibrous structure: a novel scaffold for tissue engineering. *Journal of Biomedical Materials Research: An Official Journal of The Society for Biomaterials, The Japanese Society for Biomaterials, and The Australian Society for Biomaterials and the Korean Society for Biomaterials* 60: 613-621, 2002.

42. Liao J. and I. Vesely. Relationship between collagen fibrils, glycosaminoglycans, and stress relaxation in mitral valve chordae tendineae. *Annals of biomedical engineering* 32: 977-983, 2004.

43. Liao J. and I. Vesely. A structural basis for the size-related mechanical properties of mitral valve chordae tendineae. *Journal of biomechanics* 36: 1125-1133, 2003.

44. Liao X., M. Dulle, J. M. d. S. e Silva, R. B. Wehrspohn, S. Agarwal, S. Förster, H. Hou, P. Smith and A. Greiner. High strength in combination with high toughness in robust and sustainable polymeric materials. *Science* 366: 1376-1379, 2019.

45. Merryman W. D., H. D. Lukoff, R. A. Long, G. C. Engelmayr Jr, R. A. Hopkins and M. S. Sacks. Synergistic effects of cyclic tension and transforming growth factor-β1 on the aortic valve myofibroblast. *Cardiovascular pathology* 16: 268-276, 2007.

46. Millington-Sanders C., A. Meir, L. Lawrence and C. Stolinski. Structure of chordae tendineae in the left ventricle of the human heart. *Journal of anatomy* 192: 573-581, 1998.

47. Molina C. P., R. Giglio, R. M. Gandhi, B. M. Sicari, R. Londono, G. S. Hussey, J. G. Bartolacci, L. M. Q. Luque, M. C. Cramer and J. L. Dziki. Comparison of the host macrophage response to synthetic and biologic surgical meshes used for ventral hernia repair. *Journal of Immunology and Regenerative Medicine* 3: 13-25, 2019.

48. Mondal A., R. Borah, A. Mukherjee, S. Basu, M. Jassal and A. K. Agrawal. Electrospun self-assembled nanofiber yarns. *Journal of Applied Polymer Science* 110: 603-607, 2008.

49. Mouthuy P.-A., N. Zargar, O. Hakimi, E. Lostis and A. Carr. Fabrication of continuous electrospun filaments with potential for use as medical fibres. *Biofabrication* 7: 025006, 2015.

50. Panseri S., C. Cunha, J. Lowery, U. Del Carro, F. Taraballi, S. Amadio, A. Vescovi and F. Gelain. Electrospun micro-and nanofiber tubes for functional nervous regeneration in sciatic nerve transections. *BMC biotechnology* 8: 1-12, 2008.

51. Pham Q. P., U. Sharma and A. G. Mikos. Electrospinning of polymeric nanofibers for tissue engineering applications: a review. *Tissue engineering* 12: 1197-1211, 2006.

52. Revuelta J. M., R. Garcia-Rinaldi, L. Gaite, F. Val and F. Garijo. Generation of chordae tendineae with polytetrafluoroethylene stents: results of mitral valve chordal replacement in sheep. *The Journal of Thoracic and Cardiovascular Surgery* 97: 98-103, 1989.

53. Ritchie J., J. N. Warnock and A. P. Yoganathan. Structural characterization of the chordae tendineae in native porcine mitral valves. *The Annals of thoracic surgery* 80: 189-197, 2005.

54. Ross C. J., J. Zheng, L. Ma, Y. Wu and C.-H. Lee. Mechanics and Microstructure of the Atrioventricular Heart Valve Chordae Tendineae: A Review. *Bioengineering* 7: 25, 2020.

55. Schnell E., K. Klinkhammer, S. Balzer, G. Brook, D. Klee, P. Dalton and J. Mey. Guidance of glial cell migration and axonal growth on electrospun nanofibers of poly-ε-caprolactone and a collagen/poly-ε-caprolactone blend. *Biomaterials* 28: 3012-3025, 2007.

56. Sensini A. and L. Cristofolini. Biofabrication of electrospun scaffolds for the regeneration of tendons and ligaments. *Materials* 11: 1963, 2018.

57. Sicari B. M., J. L. Dziki, B. F. Siu, C. J. Medberry, C. L. Dearth and S. F. Badylak. The promotion of a constructive macrophage phenotype by solubilized extracellular matrix. *Biomaterials* 35: 8605-8612, 2014.

58. Smit E., U. Bűttner and R. D. Sanderson. Continuous yarns from electrospun fibers. *Polymer* 46: 2419-2423, 2005.

59. Syedain Z. H. and R. T. Tranquillo. Controlled cyclic stretch bioreactor for tissue-engineered heart valves. *Biomaterials* 30: 4078-4084, 2009.

60. Tan R. H. H., R. Bell, B. Dowling and A. Dart. Suture materials: composition and applications in vetern-ary wound repair. *Australian veterinary journal* 81: 140-145, 2003.

61. Tandler J. and I. Abt. Anatomy of Heart: Handbook of Anatomy of Man. *Bandelben Gustav Fischer* 3: 84.

62. Teo W.-E., R. Inai and S. Ramakrishna. Technological advances in electrospinning of nanofibers. *Science and technology of advanced materials* 12: 013002, 2011.

63. Teo W. E., W. He and S. Ramakrishna. Electrospun scaffold tailored for tissue-specific extracellular matrix. *Biotechnology Journal: Healthcare Nutrition Technology* 1: 918-929, 2006.

64. Teo W. E. and S. Ramakrishna. A review on electrospinning design and nanofibre assemblies. *Nanotechnology* 17: R89, 2006.

65. Vetter H. Replacement of chordae tendinae of the mitral valve using the new expanded PTFE suture in sheep. *Biologic and bioprosthetic valves* 772-784, 1985.

66. Xue J., T. Wu, Y. Dai and Y. Xia. Electrospinning and electrospun nanofibers: methods, materials, and applications. *Chemical reviews* 119: 5298-5415, 2019.

67. Yan H., L. Liu and Z. Zhang. Continually fabricating staple yarns with aligned electrospun polyacrylonitrile nanofibers. *Materials Letters* 65: 2419-2421, 2011.

68. Youngstrom D. W. and J. G. Barrett. Engineering tendon: scaffolds, bioreactors, and models of regeneration. *Stem Cells International* 2016: 2016.

69. Yousefzadeh M., M. Latifi, W. E. Teo, M. Amani-Tehran and S. Ramakrishna. Producing continuous twisted yarn from well-aligned nanofibers by water vortex. *Polymer Engineering & Science* 51: 323-329, 2011.

70. Zhang L., S. Chen, R. Liang, Y. Chen, S. Li, S. Li, Z. Sun, Y. Wang, G. Li and A. Ming. Fabrication of alignment polycaprolactone scaffolds by combining use of electrospinning and micromolding for regulating Schwann cells behavior. *Journal of Biomedical Materials Research Part A* 106: 3123-3134, 2018.